PLASMA-ASSISTED DEPOSITION OF NITROGEN-DOPED AMORPHOUS CARBON FILMS ONTO POLYTETRAFLUOROETHYLENE FOR BIOMEDICAL APPLICATIONS

A Thesis Submitted to the College of
Graduate Studies and Research
In Partial Fulfillment of the Requirements
For the Degree of Doctor of Philosophy
In the Department of Physics and Engineering Physics
University of Saskatchewan
Saskatoon

By

MIKHAIL FOURSA

Keywords: plasma, deposition, amorphous carbon, nitrogen doping, blood compatibility, XPS, EELS, XAS, Raman, FTIR, AFM

Permission to use

In presenting this thesis in partial fulfillment of the requirements for a Postgraduate degree from the University of Saskatchewan, I agree that the Libraries of this University may make it freely available for inspection. I further agree that permission for copying of this thesis in any manner, in whole or in part, for scholarly purposes may be granted by the professor or professors who supervised my thesis work or, in their absence, by the Head of the Department or the Dean of the College in which my thesis work was done. It is understood that any copying or publication or use of this thesis or parts thereof for financial gain shall not be allowed without my written permission. It is also understood that due recognition shall be given to me and to the University of Saskatchewan in any scholarly use which may be made of any material in my thesis.

Requests for permission to copy or to make other use of material in this thesis in whole or part should be addressed to:

Head of the Department of Physics and Engineering Physics

University of Saskatchewan

Saskatoon, Saskatchewan S7N 5E2

Canada

Abstract

With growing demand for cardiovascular implants, improving the performance of artificial blood-contacting devices is a task that deserves close attention. Current prostheses made of fluorocarbon polymers such as expanded polytetrafluoroethylene (ePTFE) suffer from early thrombosis and require periodic replacement. A great number of attempts have already been made to improve blood compatibility of artificial surfaces, but only few of them found commercial implementation. One of the surfaces under intensive research for cardiovascular use is amorphous carbon-based coatings produced by means of the plasma-assisted deposition. However, this class of coatings can be produced using various techniques leading to a number of coatings with different properties. Carbon coatings produced in different plasmas may be of hard diamond-like type or soft graphite-like type, doping with different elements also changes the surface structure and properties. Taking this into account, the search for blood-compatible coating requires the understanding of surface composition and structure and its influence on blood-compatibility. This work attempts to advance our knowledge of this field. Here, commercial PTFE thin film was used as a working material, which composition corresponds to the composition of modern ePTFE vascular grafts and which compatibility with blood we tried to improve by deposition of nitrogenated amorphous carbon (a-CN) coatings in the plasma. Biocompatibility was assessed by a number of tests including the interaction with whole blood and various cells such as platelets, endothelial cells, neutrophils, and fibroblasts. Most of tests showed the blood compatibility of coated surface is better than that of untreated PTFE. Physico-chemical and morphological properties of coated surfaces were studied in

parallel using x-ray photoemission spectroscopy (XPS), electron energy loss spectroscopy (EELS), x-ray absorption spectroscopy (XAS), Raman spectroscopy, Fourier transform infrared spectroscopy (FTIR), atomic force microscopy (AFM). Some correlation between the structure of coatings and blood compatibility was inferred. It was found that at first nitrogen incorporation into amorphous carbon film stimulates blood compatibility. However, when nitrogen fraction increases over 23-25 %, no further improvement but reduction of blood compatibility was observed. Conclusion is made that for best biomedical performance, nitrogen percentage in a-CN coatings must be adjusted to the optimum value.

Acknowledgements

I would like to thank Dr. A.Hirose, who gave me the exciting opportunity to carry out this research at the University of Saskatchewan, who directed and supervised my work throughout this period of my career. Also, I would like to thank Dr. V.Vasilets, without whom this work would not have been possible. Many thanks to Dr. C.Xiao and Dr. Q.Yang, who offered many useful advices and discussions. The training and assistance provided by Dr. R.Sammynaiken and J.Maley at the Saskatchewan Surface Structural Center was indispensable for the success of this project. Collaboration with Dr. D.Mantovani and F.Boccafoschi at the Laval University (Quebec city), which is an essential part of this research, is appreciated very much.

Also, thanks go out to T.Hamilton and Dr. M.Yablonskikh for measuring XAS spectra at the Advanced Light Source (Berkeley, CA) and fruitful discussions. Dr. A.Adnot at Laval University (Quebec city), who measured XPS and EELS spectra, also deserves special mentioning here.

My warmest thanks to all Plasma Physics Lab members, past and present, for creating and sharing friendly working environment and helpfulness.

The research was funded by Natural Sciences and Engineering Research Council of Canada (NSERC) and by Canada Research Chair program. Financial support by the University of Saskatchewan Graduate Scholarship is also gratefully acknowledged.

Table of contents

List of tables

List of figures

List of abbreviations

a-C – Amorphous carbon

a-CN – Amorphous carbon doped with nitrogen

a-CN#1, a-CN#2, a-CN#3, a-CN#4, a-CN#5 – refer to Table 1

a-CP – Amorphous carbon doped with phosphorous

AFM – Atomic force microscopy

ALS – Advanced Light Source

CVD – Chemical vapor deposition

DC – Direct current

DDF – Depth distribution function

DLC – Diamond-like carbon

DOS – Density of states

EELS – Electron energy loss spectroscopy

EISCS – Electron inelastic scattering cross-section

ePTFE – Expanded polytetrafluoroethylene

FEP – Fluoroethylene-propylene

FTIR – Fourier-transformed infrared spectroscopy

ICP – Inductively coupled plasma

IMFP – Inelastic mean free path

IR – Infrared

ISO – International Organization for Standardization

LTIC – Low-temperature isotropic pyrolytic carbon

LTPC – Low-temperature pyrolytic carbon

MED – Mean escape depth

MSIB – Mass-selected ion beam deposition

PBS – Phosphate buffered saline

PET – Polyethylene terephthalate

PIII-D – Plasma-immersion ion implantation-deposition

PMMA – Polymethylmethacrylate

PRP – Platelet-rich plasma

PTFE – Polytetrafluoroethylene

REELS – Reflection energy loss spectroscopy

RF – Radiofrequency

RIPA – Relative index of platelet adsorption

SEM – Scanning electron microscopy

ta-C – Tetrahedrally-bonded amorphous carbon

TEELS – Transmission electron energy loss spectroscopy

TEY – Total electron yield

TFY – Total fluorescence yield

VUV – Vacuum ultraviolet

XAS – X-ray absorption spectroscopy

XPS – X-ray photoemission spectroscopy

1. Introduction

According to World Health Organization reports, cardiovascular diseases are among the most frequent causes of human death. In many cases, the only way to save life is heart transplantation or replacement of non-performing blood vessels. The replacement blood vessel often may be taken from the same patient, but in more severe cases this opportunity may not exist. Currently, the problem is partially solved by use of artificial blood vessels. Two materials most commonly used for manufacturing of vascular prostheses are Dacron and ePTFE. Dacron is a trademark registered by DuPont and used for synthetic fabric made of polyethylene terephthalate (PET). Expanded polytetrafluoroethylene (ePTFE) produced by Gore-Tex® is a porous form of well-known polymer distinguished for its outstanding properties. Unfortunately, performance of currently available prosthesis is limited because of the problems related to biocompatibility, such as surface induced thrombosis and susceptibility to infection. Investigations in this area have revealed that if the diameter of PTFE grafts is 6 mm or less, approximately 30% of the grafts are closed by thrombi and need replacement after 3 months; after 36 months, only 20% of the artificial grafts are still patent. Reduction of thrombogenicity of commercial cardiovascular prostheses is highly beneficial for patients if it is not conjugated with worsening of other biocompatible properties, such as low inflammation, cell friendliness *etc*.

A possible approach to improve blood compatibility of polymers is surface modification by means of the plasma-assisted thin film deposition. Amorphous carbon-based coating is a

good candidate for that purpose. Amorphous carbon films are obtainable by numerous plasma-enhanced deposition techniques. Blood compatibility of carbon-coated surfaces is attributed to chemical inertness and abundant presence of this element in human body. Smooth surface obtainable by the plasma-assisted deposition is expected to enhance undisturbed laminar blood flow and reduce the effect of topography on the cell adhesion to the surface. Nitrogen doping can enhance flexibility of carbon films by removing the internal stress. Nitrogen containing groups could be used for further immobilization of biomolecules.

1.1 Materials used in research

PTFE is a polymer obtained as a result of polymerization of tetrafluoroethylene molecules and its chemical formula is

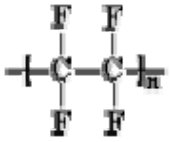

The carbon-fluorine bond is very strong (dissociation enthalpy ~450 kJ/mol) and highly non-covalent with shift toward fluorine atom which makes its outer shell complete, similar to that of the noble gases. In addition, the main chain of the polymer is twisted in such a way that it becomes tightly wrapped by fluorine atoms (Figure 1). On this basis, it's easy to realize what makes the PTFE one of the most inert and stable materials in nature.

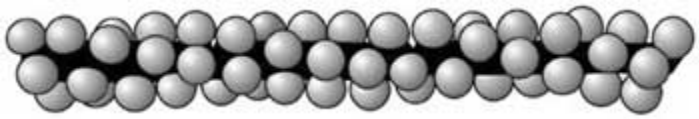

Figure 1 PTFE molecule

PTFE is commercially available as a bulk polymer, thick sheets, and thin film. For this research project, plane PTFE film of thickness 0.05 mm was chosen as a substrate material. Porosity is avoided at this stage in order to simplify treatment and analysis of modified surface.

Carbon can form a great variety of allotropes because its atom can have three bonding configurations (Figure 2).

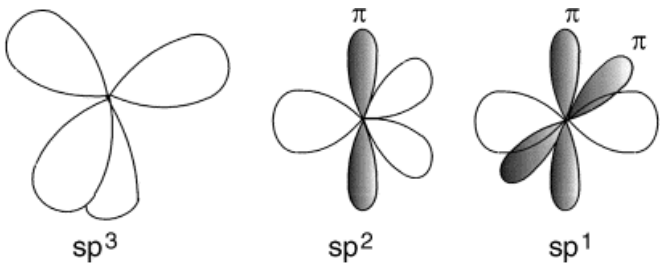

Figure 2 Bonding configurations of carbon atom

First one is tetrahedrally directed four-fold configuration of σ-type, as in diamond. Because of symmetry, all four carbon bonds in diamond are equivalent and this is called sp^3 hybridization. Second one is trigonally directed three-fold planar configuration, which contains both σ and π-type bonds. In symmetric structures like six-fold rings in graphite, π-orbitals are delocalized (electronic is equally distributed between each of six carbon atoms) and all three planar bonds are equivalent (sp^2 hybridization). Third configuration corresponds to linear geometry. In such configuration, π orbitals are always localized and σ orbitals are sp^1 hybrids. It is worth mentioning that ultimate hybridization is achieved only in perfectly symmetric configurations, which may not be the case if one or more adjacent carbon atoms are substituted by more electronegative atoms.

Carbon can form crystalline structures (diamond, graphite), as well as amorphous and molecular solids (C60). Diamond (Figure 3a) has cubic face-centered crystalline lattice. In graphite (Figure 3b), plane sheets formed by carbon six-fold rings of benzene type are connected to each other by weak Van der Waals forces. C60 or Buckminsterfullerene (Figure 3c) is a molecule that has a shape of soccer ball formed by linked hexagonal and pentagonal rings with total number of sixty carbon atoms. It should be mentioned, that fullerenes with total number of carbon atoms other than sixty also exist (C70, C540), as well as cylindrical fullerene structures called "carbon nanotubes".

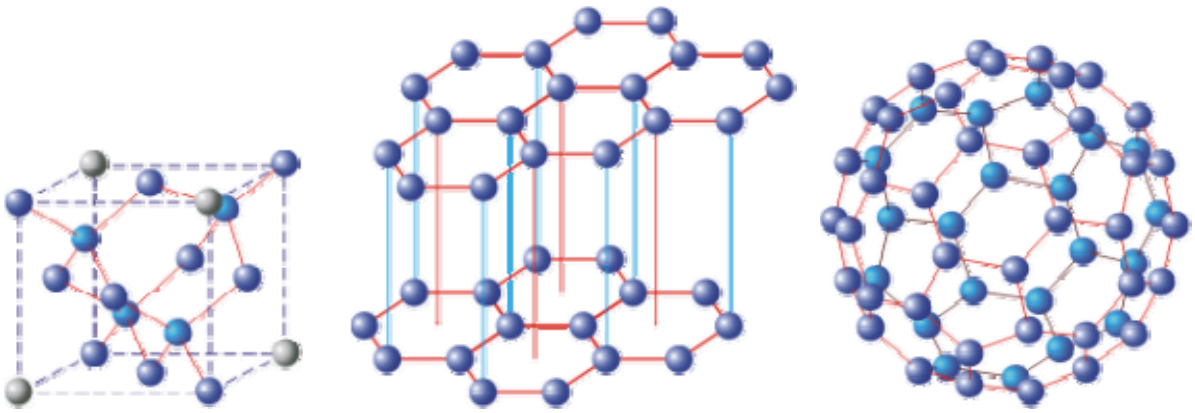

(a) diamond (b) graphite (c) C60

Figure 3 Carbon allotropes

Amorphous carbon is a material that has no crystalline structure; it may be thought of as a random network of carbon atoms, each of which may have one of three possible bonding configurations. For characterization of structure of amorphous carbons, two limiting cases are usually used as reference points. First one is graphite-like amorphous carbon. It contains a large amount of sp^2 bonded carbon which may be incorporated into six or five-fold rings

(or even nano-sized graphitic clusters). The other one is diamond-like carbon which consists mostly of sp^3 bonded carbon atoms, like diamond, but without long-range order.

Nitrogen normally has three valent electrons and a lone pair. In this case, it can have bonding configurations similar to those of carbon, where one σ-type bond is substituted by the lone pair of electrons. However, the presence of strongly negative lone pair slightly decreases the angles between bonding orbitals. In some cases, nitrogen may appear in pentavalent form. Generally, nitrogen incorporated into carbon network may have one of many possible configurations shown in Figure 4.

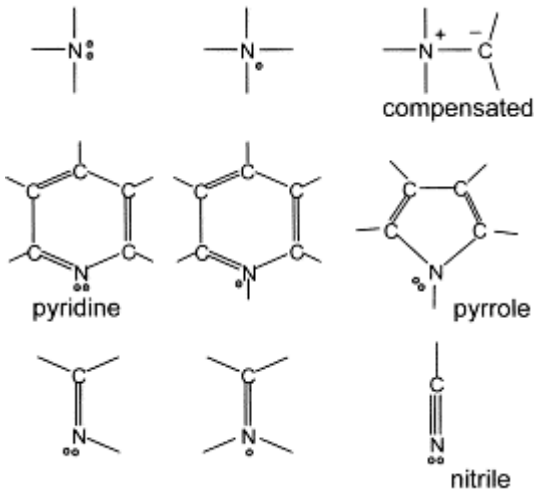

Figure 4 Various nitrogen bonding configurations in a-CN.
One dot means an unpaired electron. Two dots mean a lone pair (non-bonding).
(Robertson, 2002)

1.2 Objectives

The central objective of this work is to develop a reliable plasma coating technology to enhance blood compatibility of PTFE for cardiovascular applications. Amorphous carbon with various nitrogen doping is used as a coating material. Deposition is made onto PTFE and silicon wafers to enhance different methods of analysis. In search for a method to produce nonthrombogenic blood compatible coatings, blood compatibility must be investigated with relation to physicochemical properties of coatings. Structure and surface morphology has a great influence on blood compatibility (Black, 1999). Obtaining the correlation between those parameters and the biological performance is highly desirable and potentially helpful for ultimate goal achievement.

1.3 Thesis outline

Thesis consists of five chapters. Chapter 1 contains a brief introduction to the problem under consideration, materials used in this research, and objectives statement. Chapter 2 addresses various aspects of plasma-enhanced material processing, plasma-surface interaction, and methods for deposition of carbon-based coatings. As well, it describes experimental setup used in this project. Chapter 3 is devoted to investigation of coating structure and morphology. It is divided into sections to set apart specific techniques used for analysis: XPS, EELS, XAS, Raman and FTIR spectroscopy, and AFM. Each section of chapter 3 contains introduction to the method, experimental details, and results. Chapter 4 is devoted to blood and biocompatibility. In similar way, it contains introduction, review of latest achievements in the area of carbon-based coatings for blood compatibility improvement, and results of tests. Chapter 5 summarises all major results and draws the conclusion.

2. Plasma surface engineering

2.1 Role of plasma in material processing

Chemically reactive plasma discharges are widely used to modify the surface properties of materials. Plasma processing technology is vitally important to several of the largest manufacturing industries in the world. Plasma-based surface processing is critical for electronics, aerospace, automotive, steel, biomedical, and toxic waste management industries. In the plasma, material structure and surface properties can be engineered in unique ways. For example, plasma-based hardening of surgically implanted hip joints and machine tools significantly extends their working lifetimes. Hard coatings such as titanium carbide (TiC), titanium nitride (TiN), and aluminum oxide (Al_2O_3) are intensively used to enhance the life of cutting tools and many other components for which friction and wear are a problem. Diamond films grown by plasma-assisted deposition may have intrinsic properties almost similar to those of natural or synthetic diamond crystals, promising their use as substitute for diamond in a variety of diamond-based optical and electronic device applications (Lieberman & Liehtenberg, 1994).

2.2 Low-temperature plasma interaction with polymers

Low-temperature low-pressure plasmas are characterized by pressure p ≈ 1mTorr –1 Torr, electron temperature T_e≈ 1-10 eV, and low ion temperature $T_i << T_e$. Ionization degree is very small for such systems and usually is not higher than 10^{-5}. Although concentration of charged particles is much smaller than that of neutrals, charged particles play a central role in sustaining the discharge and enhancing chemical reactions. Because $T_e >> T_i$, it is the electrons that dissociate or ionize the feedstock gas to create free radicals, atoms, and ions which are active components of the plasma and responsible for chemical reaction on the surface of polymers being processed. Besides, energetic electrons can excite other particles, which, in turn, can decay radiationally. Plasma radiation, especially in the vacuum ultraviolet (VUV) region with the wavelengths λ = 110 nm -180 nm is also an active component of the plasma involved in chemical reactions. Intensity of such radiation can be as high as 10^{13}-10^{14} photons/cm^{2}sec depending on the conditions of discharge. Since electron and ion energies in low-temperature plasmas seldom exceed chemical bonding energy and extinction coefficients of UV radiation for most polymers are rather high, one can expect that chemical processes take place only within thin surface layer, remaining the bulk properties of material unchanged.

One of the most common processes that occur when polymer is brought into contact with plasma is surface erosion, resulting in loss of weight and thickness. It can be either a physical sputtering due to bombardment by energetic ions or a chemical etching due to reactions with active components, such as atomic oxygen, fluorine and so on. Plasma in the mixed O_2 and CF_4 is especially effective for etching and is widely used in microelectronics

for removal of photo-resist layers. Sputtering rates depend upon chemical composition and structure of polymer. Fluorocarbon polymers like PTFE and FEP show relatively lower sputtering rates compared to hydrocarbon polymers. Also, crystalline phase is less susceptible to etching than amorphous phase.

Polymers treatment by N_2 or NH_3 plasma results in formation of nitrogen-containing groups in the surface layer. Again, fluorocarbon polymers exhibit stronger resistance to this type of modification. Total nitrogen content after PTFE treatment in N_2 or NH_3 plasma usually does not exceed 6 at.% within the 10 nm surface layer, while for polyethylene, a greater value as high as 8 at.% has been achieved. Surface modification with nitrogen-containing plasma is widely used to improve biocompatibility through formation of amine groups and further immobilization of heparin and albumin.

Chemical composition and properties of modified surface can change with time after plasma treatment and exposure to atmospheric air. Mainly, this is due to post-plasma reactions of radicals and other active species with atmospheric air components and conformational rearrangement of the functional groups. This process can take a long time because it is limited by slow diffusion of atmospheric gases within solid materials and slow conformational processes (Ponomarev & Vasilets, 2000).

2.3 Plasma deposition of carbon layers onto polymers

Methods of plasma-assisted deposition of carbon-based coatings can be classified by source of carbon (hydro-carbon gases, solid graphite), or by type of discharge that is used to create plasma (DC glow, arc, RF capacitive, RF inductive, microwave, laser breakdown). Other methods where ion beam is used for direct film deposition or sputtering of graphite target also exist. All types of discharges mentioned above (except for laser-induced breakdown) utilize the idea of acceleration of free charge carriers (primarily electrons, because of their smaller mass) by the external electric field up to the energies required to ionize neutral gas particles in the collision process. Only few free electrons are required to ignite the discharge and they are normally always available due to ionization by cosmic rays or other naturally occurring radioactivity. In addition, ionization degree is always non-zero due to collisions of particles with energies corresponding to the high-energy tail of distribution function. In DC regime, discharge is sustained by constant voltage applied across the two electrodes. Electron emission from cathode also plays significant or, sometimes, crucial role for sustainability of DC discharges. Cathode emission could be due to positive ion bombardment (secondary emission), high temperature (thermionic emission), strong electric field near the cathode surface (field emission), or any combination of the above. Different types of DC discharges can be obtained depending on the applied voltage and the discharge current (Figure 5). For practical applications including materials plasma processing and thin film deposition, plasma density of about 10^9 cm^{-3} and higher is desired, which assumes larger discharge currents. From that point of view, only DC regimes from normal glow to arc deserve practical interest.

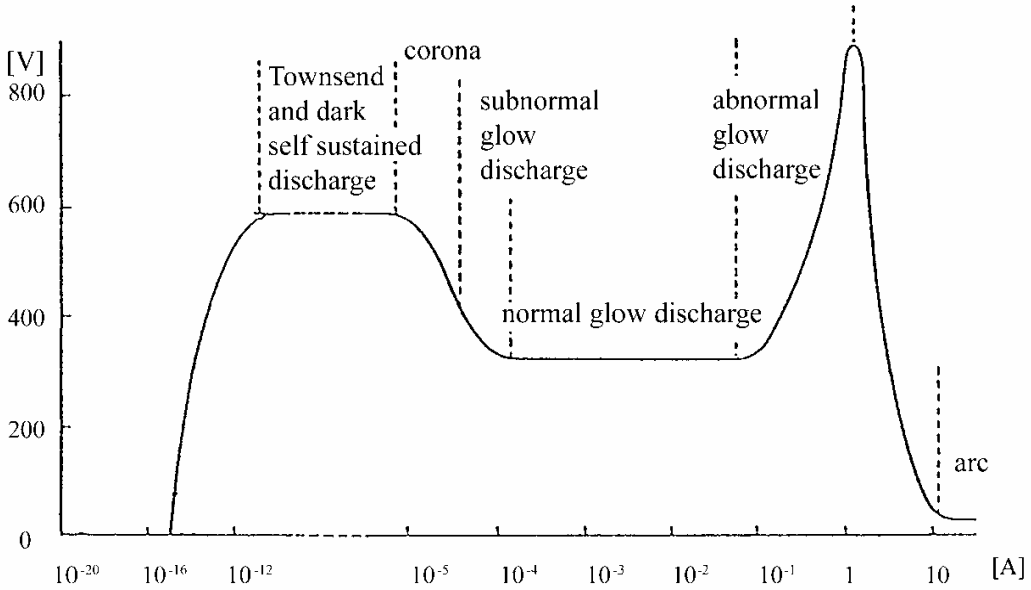

Figure 5 Voltage – current dependence for various kinds of DC discharges (Ne, 1.3 mbar, flat copper electrodes 10 cm^2, electrode distance 50 cm) (Conrads & Schmidt, 2000)

The choice of plasma source depends upon specific requirements to the process. For example, DC discharges have the advantage of simplicity because the microscopic processes in such plasmas are rather well known and understood. Microwave plasmas and inductively coupled plasmas (ICP) produced by RF inductive discharge typically provide greater plasma density (10^{11} – 10^{12} cm^{-3}), which enables higher processing rates. But the physics behind them is more complicated. Electromagnetic waves with frequencies below the electron plasma frequency,

$$\omega_{pe} = \left(\frac{n_e e^2}{\varepsilon_0 m_e} \right)^{1/2}, \qquad (1)$$

are reflected (n_e, m_e, and e stand for the electron density, electron mass, and unit charge respectively, ε_0 is the permittivity of vacuum). The electron density corresponding to the electron plasma frequency is called the cut-off density. However, the skin effect enables the penetration of the wave into the plasma to some extent. The power absorption is limited to the dimension of the skin sheath of thickness δ_s. In collisional regime, which takes place when electron-neutral collision frequency ν_{en} is higher than the frequency of electromagnetic field ω, skin depth is given by Lieberman & Lichtenberg (1994),

$$\delta_s = \sqrt{2}\frac{c}{\omega_{pe}}\left(\frac{\nu_{en}}{\omega}\right)^{1/2}, \tag{2}$$

where c denotes the velocity of light. In a non-thermal plasma with n_e~10^{10} cm^{-3} and ν_{en}~10^9 s^{-1}, the above relation gives skin depth values of 25 cm and 2 cm, respectively, for frequencies 13.56 MHz and 2.45 GHz, the two most common commercial standards for RF and microwave generators. For higher frequencies or lower gas pressures, where $\nu_{en} \ll \omega$, skin sheath is collisionless, and its depth is $\delta_s \sim c/\omega_{pe}$ (Lieberman & Lichtenberg, 1994).

RF capacitive discharge possess the capability to produce plasma with density 10^9-10^{10}cm^{-3}, which is bit less then the values achievable in ICP and microwave systems. Nevertheless, capacitive discharges are widely used in industrial and laboratory systems as relatively simple, inexpensive and reliable plasma source. The main disadvantage of RF capacitive sources is contamination due to electrode sputtering. Schematic configurations of RF-powered plasma sources are shown in Figure 6.

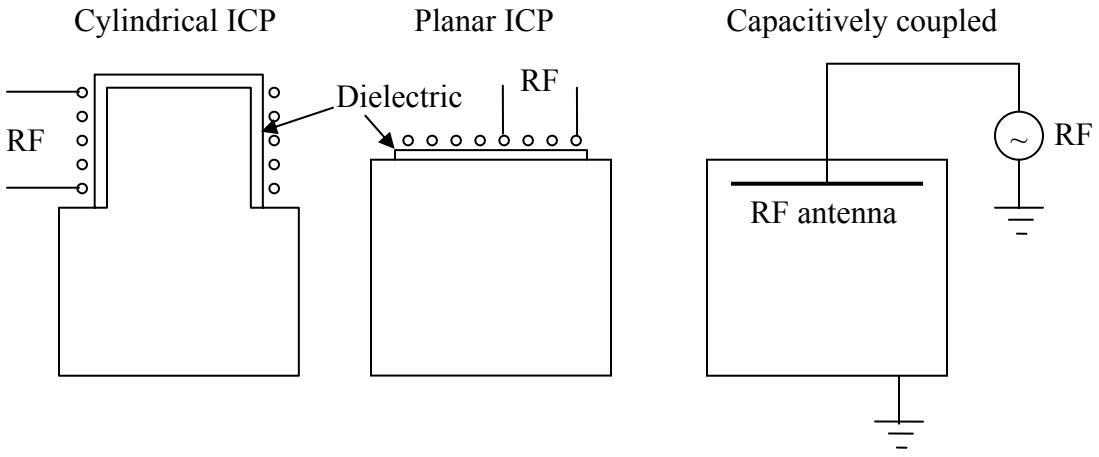

Figure 6 RF plasma sources

Most laboratory gas discharges require working pressure lower then atmospheric, which is why deposition is usually performed inside vacuum chamber which also helps to avoid undesired contamination. For production of hydrogen-free coatings graphite sputtering is preferred because the opposite method (so called "chemical vapor deposition", CVD) utilizes hydrocarbon gases and produces essentially hydrogenated coatings. To increase efficiency of sputtering process, a so called "magnetron" configuration sometimes is used (Figure 7). In such configuration, magnets are arranged behind the sputtering target with alternating polarity. Electrons become trapped as they are forced to perform spiral motion around the magnetic field lines. This increases the number of ionizing collisions and enhances plasma density near the target.

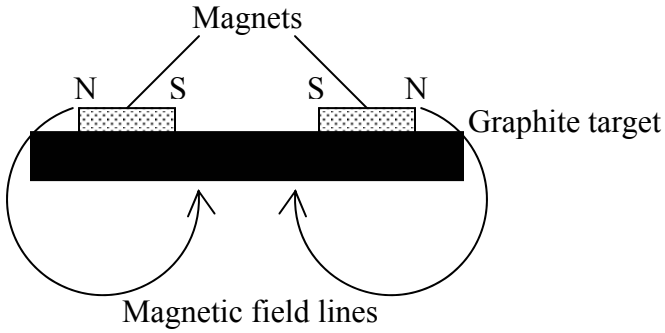

Figure 7 Magnetron sputtering configuration

Structure and properties of coatings strongly depend on the deposition technique. For example, to produce hard diamond-like carbon coating, energetic ion flux directed toward the substrate is required. The first hard amorphous carbon coatings were deposited by a beam of carbon ions produced in argon plasma on room temperature substrates (Aisenberg & Chabot, 1971). Following this work, several alternative techniques were developed. Cathodic arc and pulsed laser vaporization are the two methods to produce the hardest DLCs (Bhushan, 1999). Vacuum arc discharge between graphite cathode and grounded anode produces energetic carbon ions required for the production of DLC. Pulsed excimer lasers such as ArF-laser give very short, intense energy pulses that are used to vaporize material into the intense plasma expanding towards the substrate. The mean ion energy in such plasma is proportional to the laser fluence concentrated at the target spot and can reach values up to 100 eV or even higher (Voevodin & Donley, 1996). Compared to the above deposition methods, sputtering has a disadvantage that it can have only relatively low ratio of energetic ions to neutral species, so that it does not produce the hardest DLC films. However, sputtering method with a very high fraction of ions was developed by Schwan *et al*. (1996).

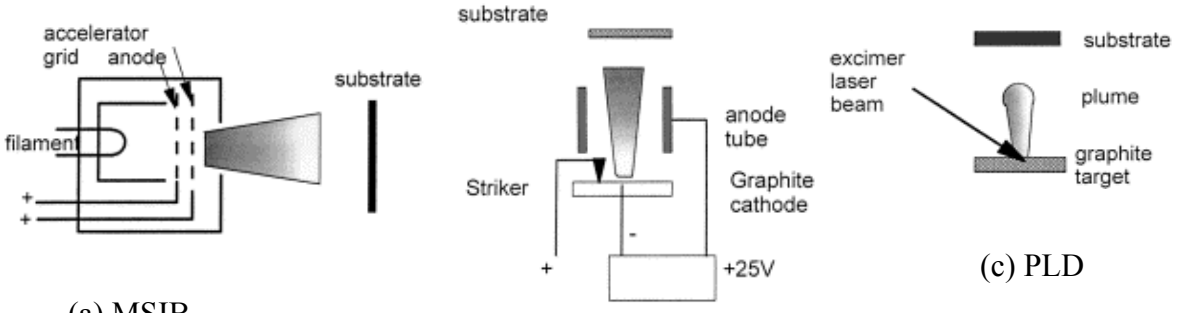

(a) MSIB

(b) Cathodic Arc

(c) PLD

Figure 8 Methods for deposition of hard DLC films
(Robertson, 2002)

For laboratory work, it is desirable to have a method which enables controlled deposition from a single ion species with well-defined ion energy. This is achieved by mass selected ion beam deposition (MSIB) (Hofsass *et al*., 1994). Carbon ions are produced in the ion source from a graphite target, such that the spread of ion energies is small, 1–10 V. The ions are then accelerated to 5–40 kV and passed through a magnetic filter. This filters out any neutrals and selects ions with an e/m ratio of the C^+ ion. The ion beam diverges because of its Coulombic repulsion. The ions are then decelerated to the desired ion energy by electrostatic lens, and the beam is focused onto the substrate in a vacuum of order 10^{-8} Torr to produce a ta-C film. The advantages of MSIB are that is gives a controllable deposition species and energy, a filtering out of non-energetic species, and the ability to dope by switching the ion species. The disadvantage is the low deposition rate of order 0.001 Å/s and the high cost of the apparatus.

2.4 Experimental details of deposition method used in this work

In this section, a hot wire plasma deposition system used by the author is described. This system was built in the Plasma Physics Laboratory and can be used for deposition of carbon films either by CVD or graphite sputtering techniques. In particular, graphite sputtering is a preferred method for deposition of a-C and a-CN films, because it can provide a hydrogen-free coating. That is not the case in CVD method in which hydrocarbon gases are usually used. Figure 9 schematically shows the system with typical parameters of deposition.

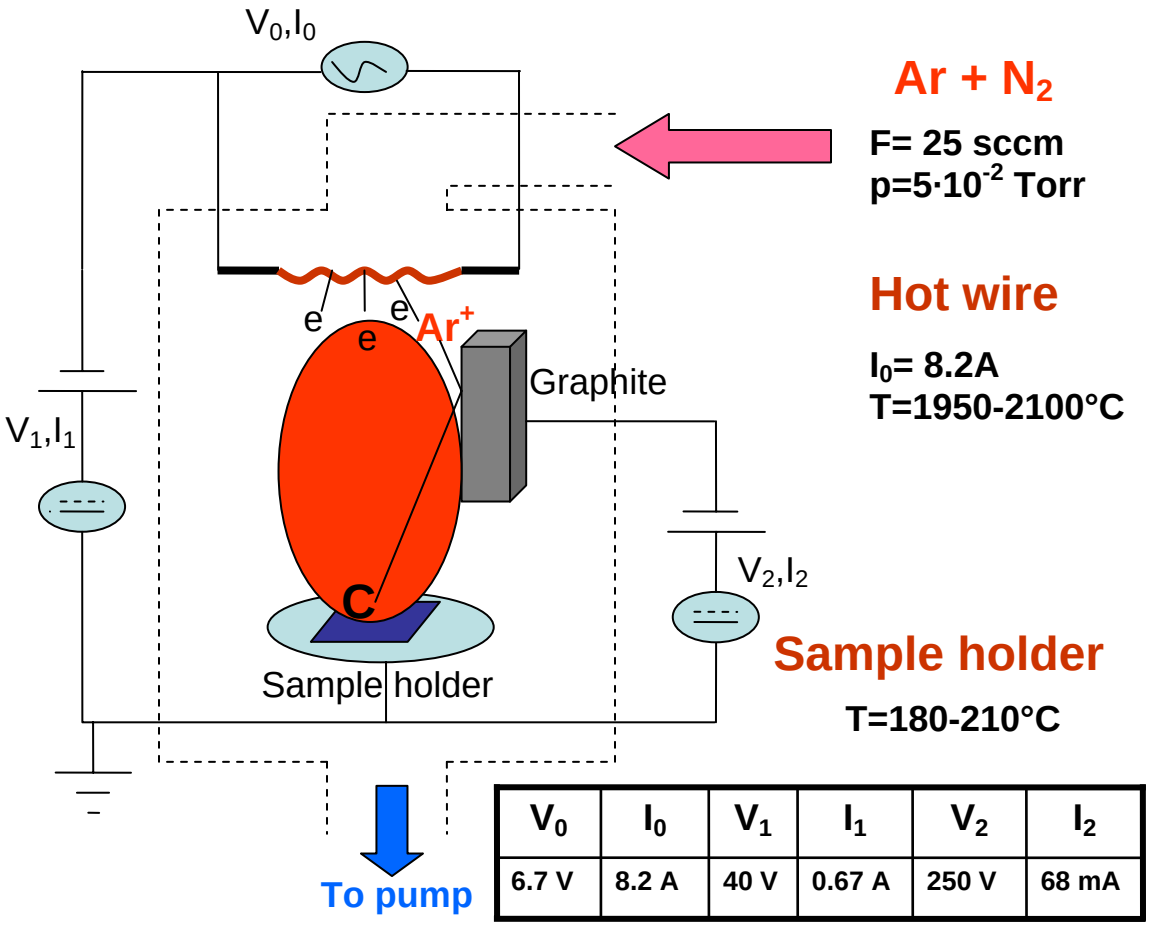

V_0	I_0	V_1	I_1	V_2	I_2
6.7 V	8.2 A	40 V	0.67 A	250 V	68 mA

Figure 9 Hot filament DC plasma deposition system with graphite sputtering target

The system utilizes tungsten wire of 0.3 mm diameter burning red-hot at about 2000°C due to 6.7 V AC applied to it and biased to -40 V as a cathode emitting electrons to produce and sustain gas discharge in the mixture of Ar and N_2 gases with flow rate of 25 sccm and working pressure of 50 mTorr. For the purpose of obtaining coatings with different nitrogen doping level, N_2 flow rate was varied in the range 0-5 sccm which corresponds to 0-20% of the total gas flow rate. Graphite target of size 2.5 cm ×2.5 cm ×1cm biased to -250 V was used as a carbon source in sputtering process. Substrate holder was about 5 cm below the hot filament and its temperature measured by thermocouple was in the range 180-210°C.

Depositions onto PTFE and Si wafer of 0.1 mm and 0.5 mm thicknesses respectively were made at the same run. While PTFE coated with a-CN is the main subject of investigations, Si-based samples were required to enable carrying out of complementary tests where usage of polymer-based samples is inappropriate (high vacuum requirements in XPS, XAS, EELS) or impossible (substrate transparency requirement in transmission FTIR). The standard deposition time of 2 hours was chosen to ensure adequate thickness and integrity suitable for advanced investigations including blood compatibility tests. Standard N_2 partial flow rates were chosen equal to 0%, 3%, 6%, 10%, and 20% of the total gas flow rate. Further consideration addresses PTFE and Si-based samples coated with a-CN under standard deposition conditions (2 hours deposition and nitrogen partial flow rates as described above). Numeration was used to identify a-CN coatings produced in such manner that a-CN#1, a-CN#2, a-CN#3, a-CN#4, a-CN#5 corresponds to 0% , 3%, 6%, 10%, 20% of N_2 partial flow rate respectively (Table 1).

Table 1. a-CN sample numeration depending on deposition parameters

Sample designation	a-CN#1	a-CN#2	a-CN#3	a-CN#4	a-CN#5
N_2 partial flow rate	0%	3%	6%	10%	20%

3. Surface characterization of plasma-treated polymers

3.1 XPS

3.1.1 Introduction

X-ray photoemission spectroscopy is a conventional technique to determine surface elemental composition. It is based on the photoelectric effect: electrons escape the surface of material after photon absorption. According to Einstein's law, the kinetic energy of an escaped free electron is less then the energy of the absorbed photon by some value which can be thought of as electron's binding energy. In typical XPS systems, energy of x-ray photons is greater than 1000 eV. Absorption of such energetic photon leads to removal of an electron from the core or other subshell atomic orbital. Binding energies of subshell electrons are specific for each element; although their chemical shift by up to 10 eV may take place, they still remain unique. Thus, the analysis of escaping electrons by their kinetic energies combined with Einstein's law gives us an idea of which elements are present in the material. Given in Figure 10 are calculated atomic subshell photoionization cross-sections for carbon and nitrogen at different photon energies (Yeh & Lindau, 1985). As one can see, for the photon energy of 1000 eV the primary photoprocess is the ionization of 1s orbitals of carbon and nitrogen which requires 285 eV and 400 eV respectively. Almost all elements can be identified by XPS except for hydrogen and helium, because photon energy of 1000 eV is too far from resonance with their ionization potentials which makes ionization

probability extremely low and brings the outgoing signal well below the sensitivity threshold of typical XPS systems.

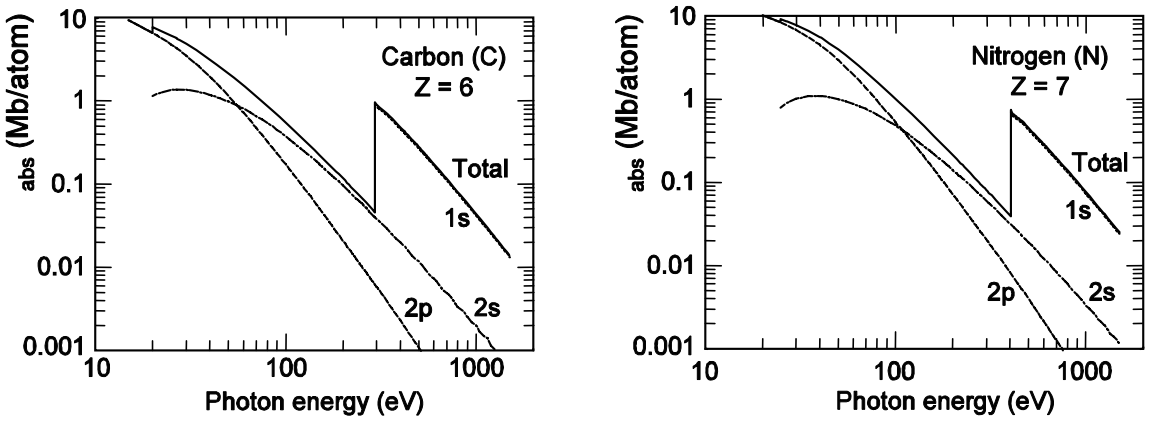

Figure 10 Atomic subshell photoionization cross-sections for carbon and nitrogen (Yeh & Lindau, 1985)

Low-resolution survey XPS spectrum typically covers large range of binding energies depending on material under investigation. Analysis of XPS spectrum involves a number of steps. First of all, spectral lines must be identified and associated with particular energy level of corresponding element. Then, the intensities of photoemission must be calculated eliminating inelastic scattering background. The necessity for presence of such background is obvious, because photoelectrons produced at various subsurface depths experience intensive inelastic scattering before escape. Two most common methods for calculating inelastic background are those proposed by Shirley (1972) and Tougaard (1988). Inelastic background calculated using one of these methods is referred to as "Shirley background" or "Tougaard background" respectively.

The method proposed by Shirley is based on the empirical assumption that the number of inelastically scattered electrons escaped within small energy interval around E is proportional to the total number of electrons with energies greater then E created in all subsurface layers. In other words, Shirley-type background $S_S(E)$ is related to the primary photoelectron spectrum $P(E)$ as it is expressed by Equation (3),

$$S_S(E) = k\int_E^\infty P(E')dE', \tag{3}$$

where k is an arbitrary constant. In practical evaluation, the measured spectrum $j(E)$ rather than the primary spectrum $P(E)$ is available, so Equation (3) is used in such a way that the primary distribution $P(E)$ is approximated as the difference of the measured intensity and some approximation to the background $S_{S,i}(E)$,

$$S_{S,i}(E) = k\int_E^\infty [j(E') - S_{S,i-1}(E')]dE'. \tag{4}$$

As initial approximation, a constant background $S_{S,0}$ is assumed. The procedure suggested by Sherwood (1983) iterates Equation (4) until the background converges.

Tougaard used more physically realistic approach. He assumed the existence of a function that described the probability of losing some energy due to an inelastic collision in function of the lost energy. A fortunate fact is that such functions can be both theoretically derived and experimentally determined. Using this formalism, Tougaard and Sigmund (1982) showed that the background $S_T(E)$ due to inelastically scattered electrons can be generated from the measured electron current $j(E)$ in one single convolution step,

$$S_T(E) = \lambda\int_E^\infty K(E' - E)\, j(E')dE', \tag{5}$$

where $K(E'–E)$ is the probability that an electron of energy E shall lose an energy $E'–E$ per unit energy and per unit path length traveled in the solid, λ is the mean free path for inelastic electron scattering.

In most practical studies, a "universal" cross-section function $K_T(T)$,

$$K_T(T) = \frac{B_T T}{(C_T + T^2)^2}, \tag{6}$$

with well-known coefficients B_T and C_T is used to calculate the Tougaard background. This function is the best fit to the average of several experimental cross-sections and it was found to describe adequately the background due to inelastic scattering in a wide range of energies and materials. It was recently shown by Vegh (2004) that the behavior of the Shirley iterated background can be reproduced by using the function $K_S(T)$,

$$K_S(T) = \frac{B_S}{C_S + T^2}, \tag{7}$$

for the inelastic energy loss cross-section. From this point of view, one shall consider the iterated Shirley background as a special case of the Tougaard background correction method, where the kernel function in the form given by Equation (7) is used.

After the inelastic background removal, correction of XPS peak intensities must be made by the sensitivity factors of the atomic energy levels, which are instrument-specific and assumed to be known from standard calibration. After correction, intensities of XPS peaks are proportional to the numbers of atoms in the analyzed volume and the calculation of atomic concentrations is straightforward.

XPS is a surface sensitive technique. The analyzed depth is defined by the mean escape depth (MED) of photoelectrons. If elastic-electron scattering is neglected, MED is equal to the electron inelastic mean free path (IMFP) multiplied by cosine of the emission angle with respect to the surface normal since depth distribution function (DDF) of the signal electrons is exponential with depth and the exponential parameter is the IMFP. Taking into account elastic collisions, MED can be changed by up to ±30% (Powell *et al.*, 1999). Electron IMFP for carbon in the energy range 700-1200 eV is about 20-30 Å as calculated by Tanuma *et al.* (1991). Figure 11 shows a compilation of measurements of the inelastic mean free path $\lambda_{in}(E)$ made by Seah and Dench (1979) in terms of atomic monolayers as a function of the kinetic energy. It can be seen from there, that the electron energy range 250-1500 eV typical for XPS corresponds to the λ_{in} range from about four to eight monolayers.

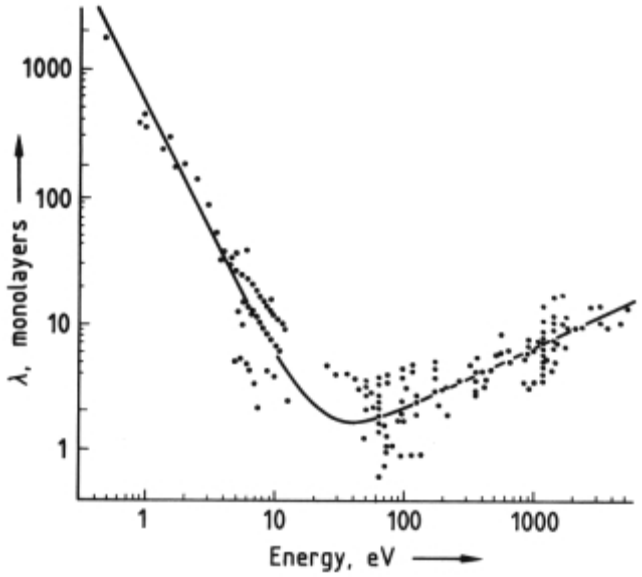

Figure 11 Electron inelastic mean free path as a function of the kinetic energy (Seah and Dench, 1979)

3.1.2 Experimental details

XPS survey spectra were measured using Kratos AXIS-ULTRA spectrometer with Al K-α monochromated x-ray source at 1486.7 eV photon energy. X-ray beam incident angle was 60 degrees with respect to the surface. Detection was performed by an 8-channel detector with energy step 1 eV. Calculation of atomic concentrations was done with CasaXPS software. All measurements and calculations were done at the Laboratory for Surface Analysis, CERPIC, Laval University (Quebec City).

3.1.3 Results

Figure 12 shows XPS survey spectra of untreated PTFE, a-CN#1, and a-CN#5. The XPS spectrum of the untreated PTFE film exhibits distinct the F1s peak (688.2 eV) and the less intense C1s peak (291.4 eV). The spectra of coated samples display intense C1s peaks (285.0 eV) as well as O1s (532.1 eV) and N1s (399.8 eV) peaks. Absence of F1s peaks in spectra of coated samples confirm the integrity of coating and suggests that its thickness is much larger then the analyzed depth.

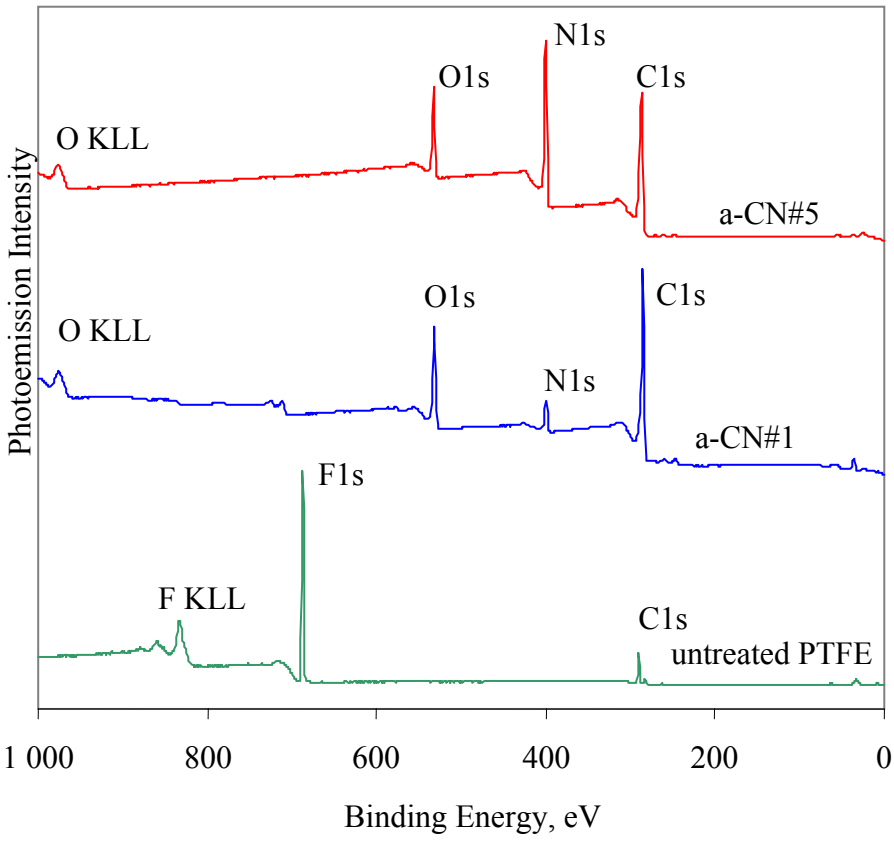

Figure 12 XPS survey spectra

Surface atomic concentrations of elements were calculated as described above and results are present in Figure 13. These data correspond to the actual composition in the surface layer of about 30 Å thick. Relatively high concentration of oxygen on the surface may be explained by post-plasma reactions after sample exposure to atmospheric air since the availability of oxygen in vacuum chamber is very limited. Bulk concentration of oxygen is expected to be much smaller.

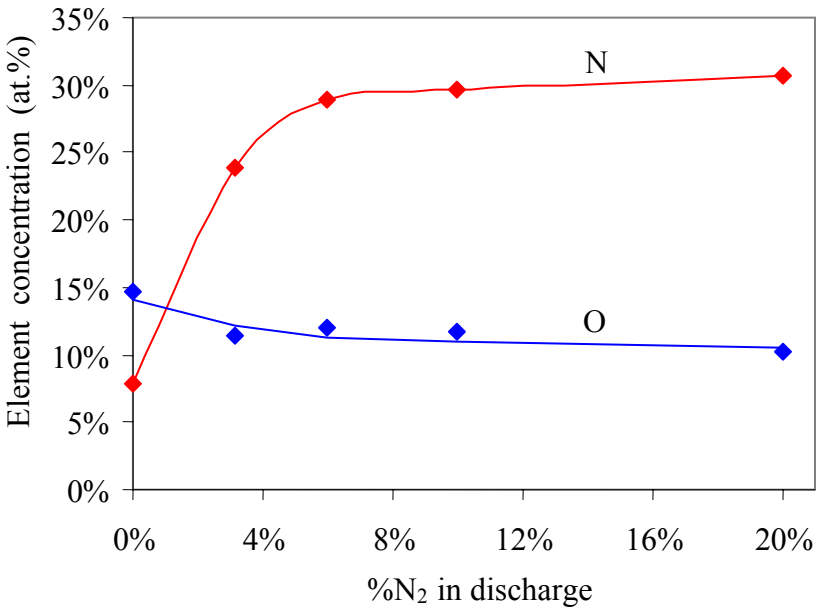

Figure 13 Surface concentration of nitrogen and oxygen in a-CN coatings
[C] ≈100%-[N]-[O]

3.2 EELS

3.2.1 Introduction

When a beam of energetic electrons passes through a layer of material, it loses part of its energy due to inelastic scattering on atomic electrons of material. Two experimental configurations are used for EELS measurements: transmission and reflection. Transmission EELS (TEELS) is experimentally more complicated. It requires preparation of thin samples, high energy and intensity of the electron beam. As it was mentioned in the previous section, inelastic mean free path of electron in carbon is only about 30 Å at the electron energy 1 keV; at the electron energy 100 keV IMFP is about 600 Å. Reflection EELS (REELS) is easier for experimental realization. It does not require special sample preparation and the typical energy of the electron beam is about 1 keV. Different angles for incidence and collection may be chosen.

Energy losses less then 100 eV are associated with excitation of valence electrons. Term "plasmons" is used for such excitations by analogy with oscillations in the gaseous plasma. Indeed, valence electrons in many metals could be considered as nearly free and their behavior is very similar to that of electrons in the plasma. Although valence band electrons in semiconductors are hardly considered as free, term "plasmons" is used with respect to semiconductors also.

In the simplest model, plasma oscillation frequency is given by Equation (1). In more detailed consideration, plasmon spatial dispersion must be taken into account,

$$\omega_p(k) = \omega_p + \alpha \frac{\hbar k^2}{2m}, \tag{8}$$

where k is plasmon wave vector (which is associated with momentum transfer), m is electron mass. The coefficient α is related to the effective mass of the electrons, so that for metals (assuming free electrons) α=1 and for insulators α=0. After introduction of spatial dispersion of plasmons, the complex dielectric function $\varepsilon = \varepsilon_1 + i\varepsilon_2$ becomes dependent not only on energy but also on momentum transfer.

The imaginary part of the negative reciprocal dielectric function,

$$\mathrm{Im}\left(-\frac{1}{\varepsilon}\right) = \frac{\varepsilon_2}{\varepsilon_1^2 + \varepsilon_2^2}, \tag{9}$$

is called "loss function" because it is closely related to electron energy losses. For an infinite medium, differential inelastic scattering cross-section per atom can be evaluated directly from the loss function,

$$\frac{d\sigma_{in}}{d\omega} = \frac{\hbar}{\pi E_0 a_0 N} \int_{k_-}^{k_+} \frac{dk}{k} \mathrm{Im}\left(\frac{-1}{\varepsilon(k,\omega)}\right), \tag{10}$$

where E_0 is the primary electron energy, $\hbar\omega = \Delta E$ is the energy loss, a_0 is the Bohr radius, N is the number of atoms per unit volume.

Integration must be done over all values of momentum transfer allowed by energy-momentum conservation, therefore the limits of integration are

$$k_{\pm} = \frac{2m}{\hbar^2}\left(\sqrt{E_0} \pm \sqrt{E_0 - \hbar\omega}\right). \tag{11}$$

More accurate consideration takes into account the excitation of surface two-dimensional plasmons and the effect of REELS geometry. Formulas for calculation of inelastic cross-section become then much more massive and can be found in the papers of Yubero & Tougaard (1992) and Yubero *et al.* (1996).

Dielectric function of a material is unknown in many cases and thus model function should be used for calculation of the inelastic scattering cross-section. Prieto *et al.* (2004) used loss function parametrized in terms of an expansion of Drude-Lindhard-type oscillators,

$$\mathrm{Im}\left(-\frac{1}{\varepsilon(k,\omega)}\right) = \sum_i \frac{A_i \gamma_i \hbar\omega}{((\hbar\omega_{pi})^2 - (\hbar\omega)^2)^2 - \gamma_i^2(\hbar\omega)^2}, \tag{12}$$

where ω_{pi} has the form given by Equation (8), $\hbar\omega = \Delta E$ is the energy loss, A_i is the oscillator strength, and γ_i is the damping coefficient. Summation must be done over all oscillator types, number of which is to be determined empirically.

On the other hand, inelastic scattering cross-section can be reconstructed from experimentally measured REELS spectrum, but before that, elastic peak must be separated from spectrum. Tougaard (2000) compared two conventional methods for inelastic background calculation in XPS (these methods are described in Section 3.1) and found that neither of them is suitable for REELS. The Shirley background (Figure 14a) gives too low elastic peak area. The Tougaard method gives too high elastic peak area because the applied

cross-section does not include surface plasmon excitations, and as a result, the intensity from surface plasmon excitation is clearly visible in the elastic spectrum (Figure 14b).

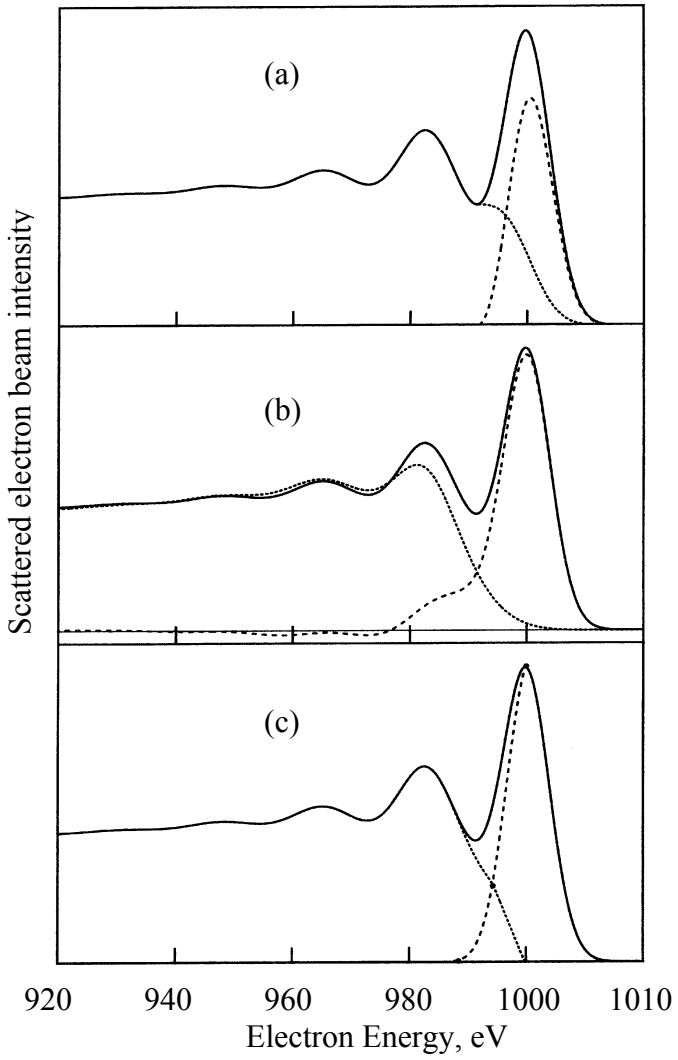

Figure 14 Different methods for elastic peak separation in REELS

On the other hand, Tougaard (2000) noticed that separation of elastic component must be easier in REELS than in XPS, because in REELS the extension of the elastic peak is determined just by the energy width of the primary electron beam and the spectrometer

energy resolution. Based on that idea, he proposed new simple method for elastic peak separation. Specifically, the method is based on the following assumptions:

I. The elastic peak is almost symmetrical.

II. It is slightly asymmetric being wider on the high-energy side (this is to some extent expected for the electron energy distribution around the hot filament).

III. The inelastic background is approximately linear with energy loss for a small energy loss and that it is zero at zero energy loss.

The example of method implementation is shown in Figure 14c.

According to Equation (5), inelastic part $j_{in}(E)$ can be calculated from the measured spectrum $j(E)$. Now we can rewrite it in the form

$$j_{in}(E) = \lambda \int_{E}^{E_0^+} K(E' - E)[j_{el}(E') + j_{in}(E')]dE' . \quad (13)$$

Introduced in Section 3.1, the value $K(\Delta E)$ is the probability that an electron loses the energy ΔE per unit energy loss per unit path length in the solid. This value is related to the differential inelastic electron scattering cross-section given by Equation (10),

$$K = \frac{N}{\hbar}\frac{d\sigma_{in}}{d\omega} . \quad (14)$$

The integration in the Equation (13) is limited to the high-energy end of the elastic peak E_0^+. For the elastic part of the integral in the right-hand side of the Equation (13), lower integration limit may be set to low-energy end of the elastic peak E_0^-, since $j_{el}(E) \equiv 0$ if $E > E_0^-$. Similarly, higher integration limit for the inelastic part of the integral in the right-hand side of the Equation (13) may be set to E_0. In general, λ and K depend on the kinetic

energy, but in the typical energy range 900-1000 eV this dependence may be ignored. Then, the elastic part of integral in the right-hand side of the Equation (13) is just a product of λ, K, and the elastic peak area A_{el}, and Equation (13) may be rewritten,

$$\lambda K(E_0 - E) = \frac{j_{in}(E) - \lambda \int_{E}^{E_0} K(E' - E) j_{in}(E') dE'}{A_{el}}, \tag{15}$$

where $A_{el} = \int_{E_0^-}^{E_0^+} I_{el}(E') dE'$. In practice, measured spectrum is not continuous, but divided into energy channels E_n with energy step E_{step} ~0.1 eV. So, integration in Equation (15) must be substituted by summation,

$$\lambda K(E_0 - E_n) = \frac{j_{in}(E_n) - \lambda \sum_{m=1}^{n-1} K(E_m - E_n) j_{in}(E_m) E_{step}}{A_{el}}. \tag{16}$$

If we note that $K(E_m - E_n) = K(E_0 - E_{n-m})$ and set p=n–m, then

$$\lambda K(E_0 - E_n) = \frac{j_{in}(E_n) - \lambda \sum_{p=1}^{n-1} K(E_0 - E_p) j_{in}(E_{n-p}) E_{step}}{A_{el}}. \tag{17}$$

Equation (17) gives the explicit recursive formula for calculation of the inelastic scattering cross-section from the inelastic part of REELS.

3.2.2 Results and discussion

REELS spectra of graphite and different CN coated surfaces are shown in Figure 15. Spectra were taken in reflection geometry with primary electron beam energy 1000 eV. Each spectrum had two prominent inelastic peaks. Higher energy loss peak at about 972 eV corresponds to plasmon excitation of all valence electrons (σ+π), and lower energy loss peak of about 991 eV corresponds to plasmon excitation of π electrons only (Waidmann *et al.*, 2001).

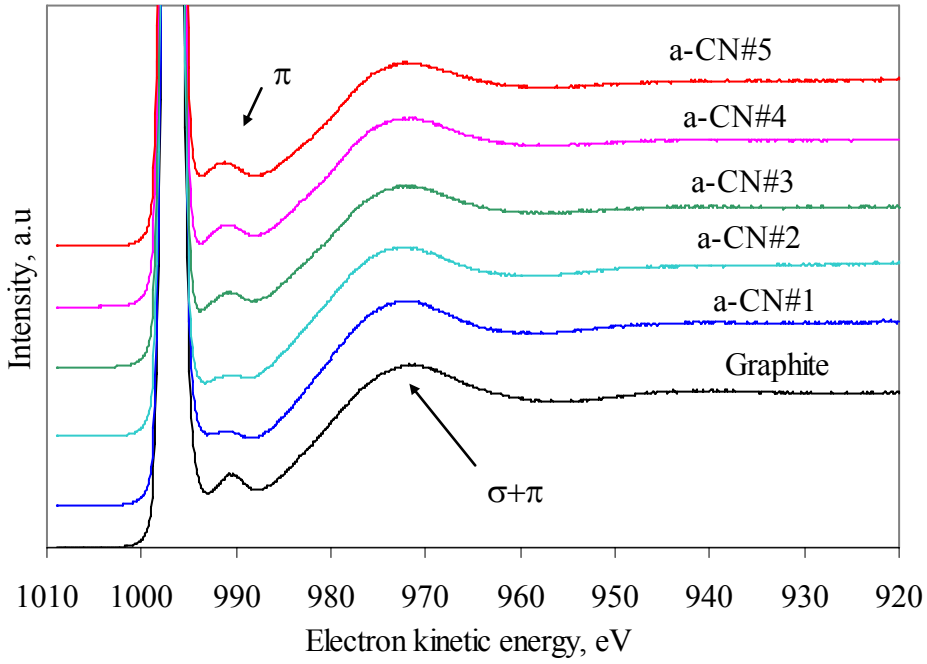

Figure 15 EELS spectra of graphite and a-CN coatings

The elastic peak was separated and inelastic electron scattering cross-section was calculated for each REELS spectrum according to procedure established by Tougaard (2000).

After that, new energy scale was introduced starting from the maximum of the elastic peak. After that, EISCS was calculated according to the Equation (10) using loss function in the form given by Equation (12); unknown parameters of loss function was varied in order to obtain the best fit of calculated EISCS to the one obtained from experimental REELS. As long as only two prominent peaks appeared in the energy loss spectra (higher energy overtones were not of interest), summation in the Equation (12) had only two terms. One term corresponded to π-type oscillators with ω_p^{π} and the other one corresponded to (σ+π)-type oscillators with $\omega_p^{\sigma+\pi}$. These plasma frequencies were the most important parameters of fit because they gave the number of π-electrons and the total number of electrons per unit volume according to the Equation (1).

During the fitting procedure, it was found that for better fit, the *k*-dispersion of plasmons must be very weak with $\alpha \lesssim 0.02$ in Equation (8). Further reduction of α did not affect the goodness of fit which means α remained uncertain in the range $0 \leq \alpha \lesssim 0.02$. For the purpose of comparison, calculations were repeated with α=0; in this case Equation (10) for calculation of inelastic scattering cross-section reduced to

$$\frac{d\sigma_{in}}{d\omega} = \frac{\hbar}{\pi E_0 a_0 N} \mathrm{Im}\left(\frac{-1}{\varepsilon(\omega)}\right) \ln\left(\frac{\sqrt{E_0} + \sqrt{E_0 - \hbar\omega}}{\sqrt{E_0} - \sqrt{E_0 - \hbar\omega}}\right). \tag{18}$$

Results of fitting are shown in Figure 16. No care was taken to include weak higher energy overtone in calculations since only the energies of π- and (σ+π)-plasmons were of interest.

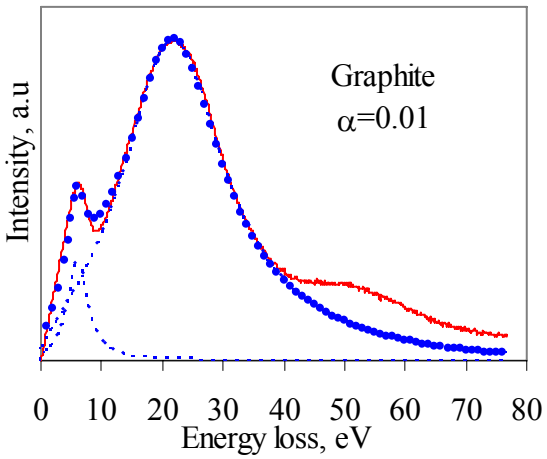
Graphite
α=0.01
Intensity, a.u
0 10 20 30 40 50 60 70 80
Energy loss, eV

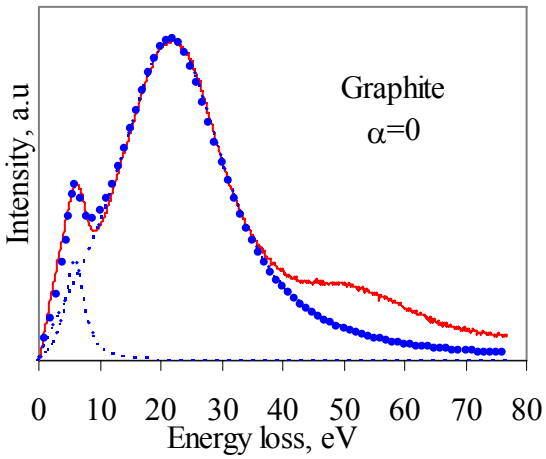
Graphite
α=0
Intensity, a.u
0 10 20 30 40 50 60 70 80
Energy loss, eV

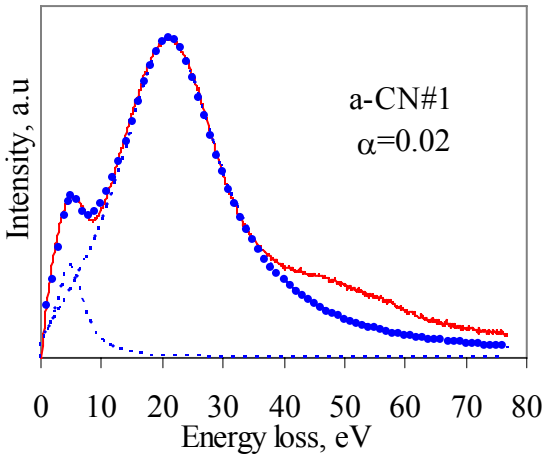
a-CN#1
α=0.02
Intensity, a.u
0 10 20 30 40 50 60 70 80
Energy loss, eV

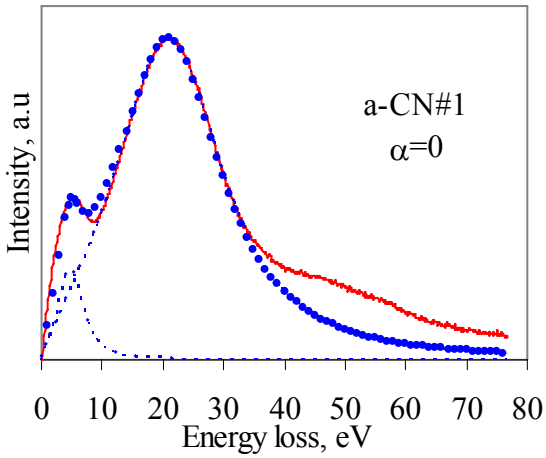
a-CN#1
α=0
Intensity, a.u
0 10 20 30 40 50 60 70 80
Energy loss, eV

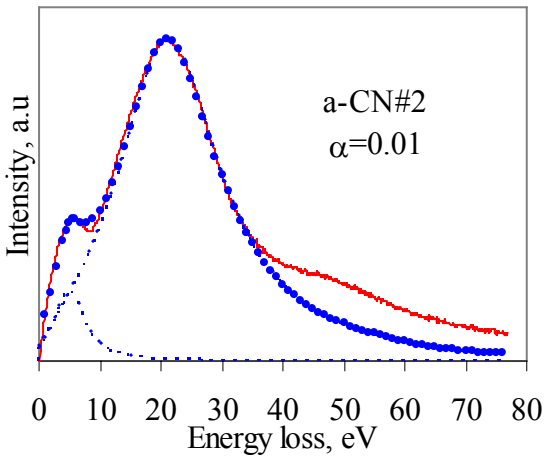
a-CN#2
α=0.01
Intensity, a.u
0 10 20 30 40 50 60 70 80
Energy loss, eV

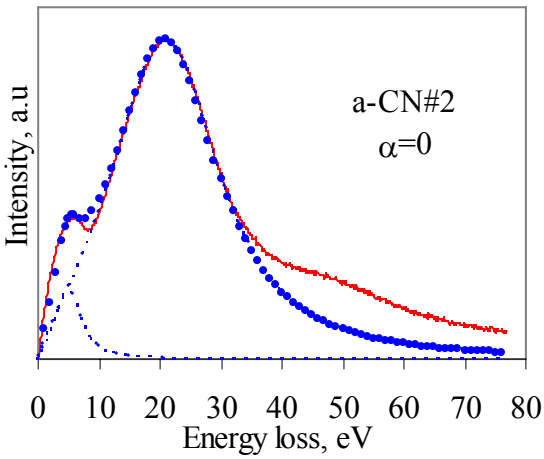
a-CN#2
α=0
Intensity, a.u
0 10 20 30 40 50 60 70 80
Energy loss, eV

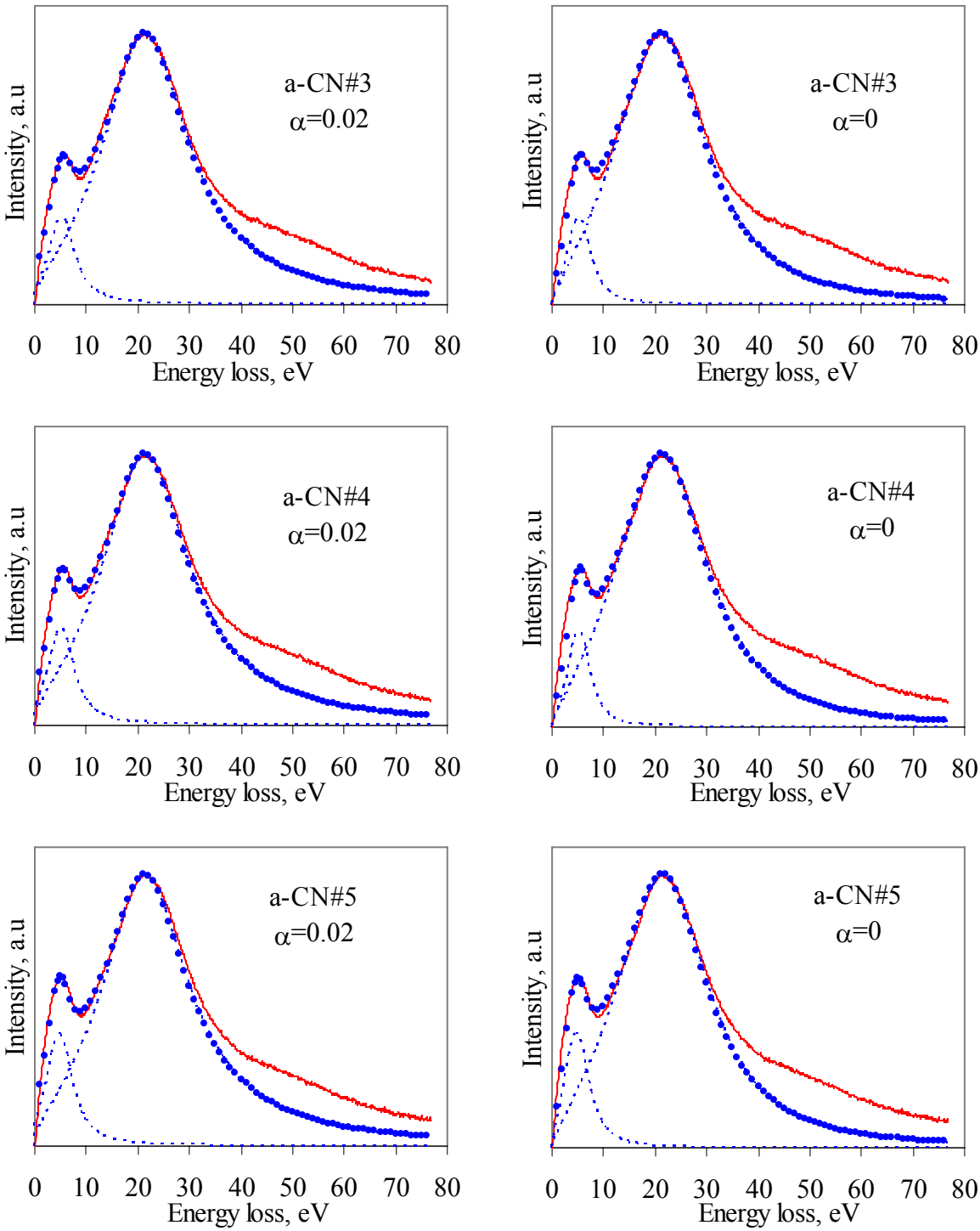

Figure 16 EELS data fitting

(Solid line corresponds to experimental data; dotted line corresponds to fitted data; dashed lines represent the individual contribution of Drude-Lindhard oscillators).

The plasmon energies obtained from the fit with α=0 and α~0.01 were slightly different (Table 2). This is understandable since $\alpha \frac{(\hbar k)^2}{2m} \sim \alpha E_0 \sim 10\ eV$, which means that even for such small α contribution of momentum transfer to plasmon dispersion is still significant in Equation (8).

Table 2. EELS plasmon energies and related parameters

Sample	Graphite		a-CN#1		a-CN#2		a-CN#3		a-CN#4		a-CN#5	
α	0.01	0	0.02	0	0.01	0	0.02	0	0.02	0	0.02	0
$\hbar\omega_p^{\pi}(eV)$	6.2	6.2	5.4	5.4	5.7	5.6	5.9	5.9	5.8	5.8	5.5	5.6
$\hbar\omega_p^{\sigma+\pi}(eV)$	23.5	24.7	22.9	24.0	23.0	23.9	23.1	24.2	23.1	24.4	23.1	24.5
$N^{\pi}/N^{\sigma+\pi}$	0.264	0.251	0.236	0.225	0.248	0.234	0.255	0.244	0.251	0.238	0.238	0.229

It can be concluded from the Table 2, that fitting with α=0 gave more accurate values of plasmon energies since it gave the relative number of π-electrons 0.251±0.004 for graphite, whereas the other method gave the value 0.264±0.004 which is too far from the true value. Accuracy of these calculations was determined by the uncertainty of π-plasmon energy which was found to be about 0.1 eV during fitting procedure.

The total number of electrons per unit volume can give estimate of mass density of coating assuming that atomic concentrations of elements are known from XPS. First, the average number of atoms per unit volume, $\overline{N}_{at}$, can be calculated,

$$\overline{N}_{at} = \frac{N_{el}^{\sigma+\pi}}{4\cdot[C]_{at} + 3\cdot[N]_{at} + 2\cdot[O]_{at}}, \tag{19}$$

where $\overline{N}_{el}^{\sigma+\pi}$ is the total number of valent electrons per unit volume, $[X]_{at}$ denotes the relative atomic concentration of element *X*, and numbers 4, 3, 2 are the numbers of valent electrons per atom in carbon, nitrogen, and oxygen respectively. In general, nitrogen can have configurations with 5 valent electrons, but formation of such configurations requires high energy impact during deposition process which is not expected under the conditions typical for the deposition system used in this research. If $\overline{N}_{at}$ is known, mass density ρ can be calculated,

$$\rho = m_u \overline{N}_{at} \left\{ 12 \cdot [C]_{at} + 14 \cdot [N]_{at} + 16 \cdot [O]_{at} \right\}, \tag{20}$$

where m_u is the unit atomic mass, and numbers 12, 14, 16 are relative atomic masses of carbon, nitrogen, and oxygen respectively. Results of mass density estimations are shown in Table 3. It should be noted, that these values were related to the thin (10-20 Å) surface layer and might differ from bulk values.

Table 3. a-CN samples surface mass densities

Sample	a-CN#1	a-CN#2	a-CN#3	a-CN#4	a-CN#5
Mass density (g/cm^3)	2.43	2.52	2.65	2.70	2.70

For pure carbon materials the relative number of π-electrons divided by 0.25 immediately gives the percent of sp^2 bonded carbon, which is not the case for doped films since atoms of doping elements may also contribute to the π-plasmon. Contributions of individual elements to the total number of π-electrons per unit volume can not be resolved using EELS.

3.3 X-ray absorption spectroscopy

3.3.1 Introduction

In XAS, the absorption of x-ray photon is associated with electron transition from core level (or other subshell level) to an unoccupied higher energy state which may be either a discrete or a continuum state. Intensity of x-ray absorption within a small energy interval ΔE at the particular wavelength is proportional to the number of vacant states lying within this energy interval in the analyzed volume. Therefore, XAS is a technique for measuring the density of unoccupied states.

$$I_{abs}(E,\Delta E) \propto \Delta N_{unocc}(E,\Delta E) \tag{21}$$

Various processes associated with x-ray photon absorption can be better explained using schematic representation of electron energy levels (Figure 17).

Resonant core electron transition to an unoccupied discrete energy level is shown in Figure 17a. Core level photoionization (Figure 17b) is also possible, if the photon energy is higher than core ionization potential. Valence photoionization (Figure 17c) is a much less intense process at photon energies near the core ionization potential (Figure 10 from Section 3.1 may be used to compare the probabilities of core photoemission and valence photoemission at the particular photon energy).

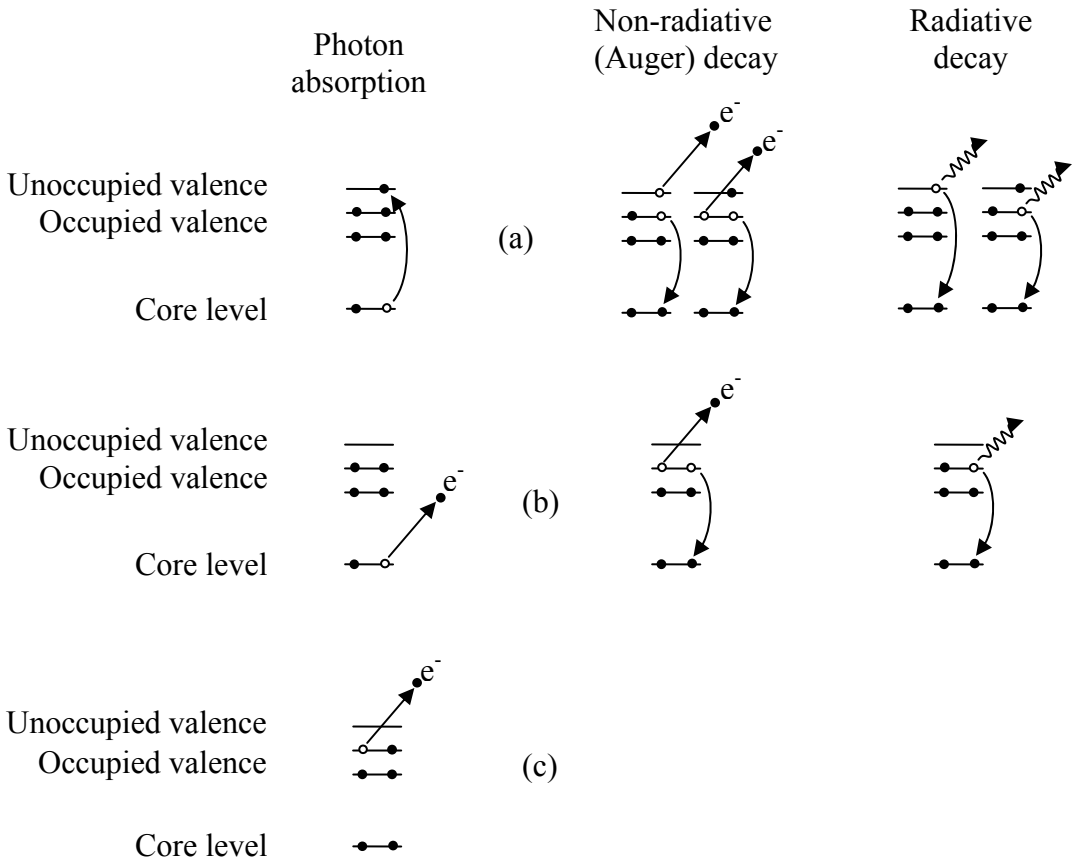

Figure 17 X-ray excitation and deexcitation processes
(Bruhwiler *et al.*, 2002)

XAS spectra are recorded by measuring the intensity of the core hole decay process. For non-radiative decay, it is the electron current; for radiative decay, it is the fluorescence intensity. Decay processes are also schematically shown in Figure 17. For light elements, non-radiative channel of core hole decay is dominant (99.7% for C and 99.5% for N) (Krause, 1979). If electron current is used for the absorption spectra registration, then the method is strongly surface sensitive because Auger electron escape depth is about 10-15 Å. Two most simple and therefore most common methods for XAS spectra registration are total electron yield (TEY) and total fluorescence yield (TFY). TEY measures electron current

running towards the sample through the substrate holder to compensate the electron loss due to Auger processes and photoionization. TFY uses photodetector to register photons escaping from sample surface with no regard to wavelength. Fluorescence yield measurements are more bulk sensitive. For characteristic x-ray photoabsorption cross-sections given in Figure 10, the corresponding photon escape depth may be estimated at 0.1 – 1 μm.

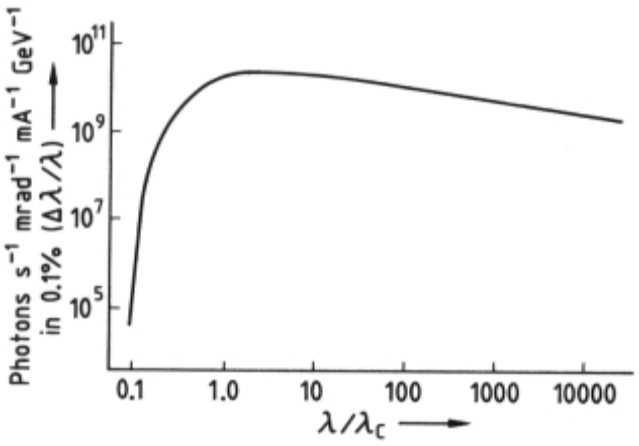

Figure 18 Normalized spectrum of synchrotron radiation.
λ_c is characteristic wavelength for the individual synchrotron (Bubert *et al.*, 2002).

XAS requires powerful and tunable x-ray source such as synchrotron. In a synchrotron, electrons are accelerated to near relativistic velocities and constrained magnetically into circular paths. When a charged particle is accelerated, it emits radiation. When near-relativistic electrons are forced into curved paths, they emit photons over a continuous spectrum. The general shape of the spectrum is shown in the Figure 18. For a synchrotron with energy of several gigaelectronvolts and the radius of some tens of meters, the energy of emitted photons near the maximum is of the order of 1 keV, and the full range of photon energies covered by synchrotron spectrum extends from far infrared to hard x-ray region.

3.3.2 XAS spectra of carbon allotropes

Typical XAS spectra of most common carbon allotropes are shown in Figure 19. Unoccupied electronic states in these materials include π* antibonding states, σ* antibonding states, and continuum states above the ionization potential ($E \gtrsim 290$ eV). π* states have lower energies (285-290 eV) then σ* states (290-320 eV), but the distinct border between them may not exist.

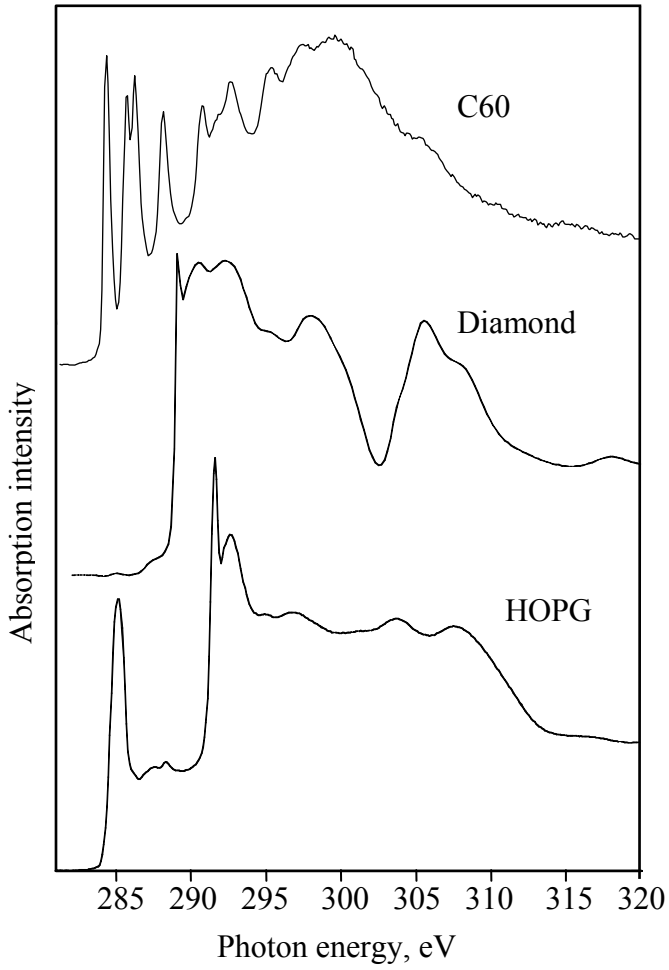

Figure 19 C1s absorption spectra of carbon allotropes

3.3.3 Quantitative analysis of XAS spectra

XAS is element selective since core electron binding energies are distinct for each element. This gives an opportunity to resolve unoccupied electronic DOS for each element. (Which is not possible with low energy EELS as discussed in Section 3.2). For amorphous carbon coatings, the key parameter defining the material properties is the relative amount of sp^3-bonded carbon atoms with respect to the amount of sp^2-bonded carbon atoms. This parameter is closely related to the relative number of π-electrons (number of π-electrons divided by total number of valent electrons) in carbon atom. If this number is equal to 0.25, then 100% of carbon is in sp^2 configuration (like in graphite or C60). Number of π-electrons per carbon atom may be estimated from XAS. According to Equation (21), integration of x-ray absorption intensity over the photon energy within some interval gives the value proportional to the number of unoccupied states lying within this energy interval in the analyzed volume. If there is a way to isolate π* and σ* features in XAS spectrum, then their integral intensities (I^{π}, I^{σ}) may be compared to the values (I^{π}_{ref} , I^{σ}_{ref}), obtained from a reference material with 100% sp^2-hybridized carbon. Then, the percentage of sp^2-bonded carbon can be calculated as

$$\%sp^2 = 100\% \frac{I^{\pi}}{I^{\pi} + I^{\sigma}} \left(\frac{I^{\pi}_{ref}}{I^{\pi}_{ref} + I^{\sigma}_{ref}} \right)^{-1`} . \qquad (22)$$

To isolate π* and σ* contribution, x-ray absorption spectrum is usually fitted by a number of Gaussian peaks, and core-level ionization is taken into account by implementation of step-like function with onset around 290 eV (Diaz *et al*., 2001). Hamilton *et al*. (2006)

suggested that exponential decay must be applied to the ionization step in order to correctly reproduce the behavior of ionization cross-section.

3.3.4 Experimental details

XAS measurements were performed at the Beamline 8.0.1 of the Advanced Light Source (ALS) at Lawrence Berkeley National Laboratory by Trent Hamilton, University of Saskatchewan M.Sc. student (2002-2005). Absorption spectra of a-CN#1 – a-CN#5 are measured in total electron yield (TEY) mode, and are normalized to the incident beam current, monitored by a high-transmission gold mesh located in front of the sample. Spectra near carbon and nitrogen absorption edge were recorded.

3.3.5 Results and discussion

Results of x-ray absorption spectra fitting are shown in Figure 20-Figure 25. In all spectra, three π^* peaks are identified. The number of σ^* peaks involved in fitting was chosen to be the minimum number required to obtain a reasonably good fit, so they may not correspond to the DOS of actual σ^* orbitals. This is a typical situation in the core-level spectroscopy, where π^* features can be identified more or less reliably, but the identification of σ^* features is not straightforward. The height of ionization step is adjusted to match the absorption intensity at 320–325 eV. In such model, exponential decay of ionization step is not significant within the given energy window. Intensities of all peaks were calculated by integration. Absorption spectrum of reference sample was processed in the same manner (Figure 25). Here, microcrystalline (μc) graphite was chosen as reference. This eliminated

the problem of angular dependence of XAS typical for highly-oriented graphite (Skytt *et al*., 1994). Based on peak areas obtained from fitting, the percentage of sp^2-bonded carbon was calculated for samples a-CN#1 – a-CN#5 according to the Equation (22) (results are shown in Table 4).

Table 4. XAS spectra fitting results

Sample	π* peak position	Partial peak area		%sp^2 carbon
		each of three	total of three	
a-CN#1	285.0 eV 286.7 eV 288.1 eV	3.6% 1.8% 1.0%	6.4%	67%
a-CN#2	285.4 eV 286.5 eV 287.5 eV	2.8% 0.8% 3.3%	6.8%	72%
a-CN#3	285.7 eV 286.5 eV 287.6 eV	2.4% 0.7% 4.1%	7.2%	76%
a-CN#4	285.6 eV 286.5 eV 287.5 eV	2.3% 0.7% 4.7%	7.7%	81%
a-CN#5	285.6 eV 286.5 eV 287.5 eV	2.4% 0.7% 4.5%	7.7%	80%
μc-graphite	285.2 eV 287.3 eV 288.8 eV	2.9% 4.5% 2.1%	9.5%	100%

The error of such calculations was estimated by Hamilton (2005) to be 4-7%. But the difference between results presented in figure Table 4 and those published by Hamilton (2005) and Hamilton *et al.* (2006) is still bigger than that. Thus, it may be concluded that the choice of reference sample for sp^2-bonded carbon evaluation may affect the result significantly. Therefore, the results obtained from such calculations require careful interpretation.

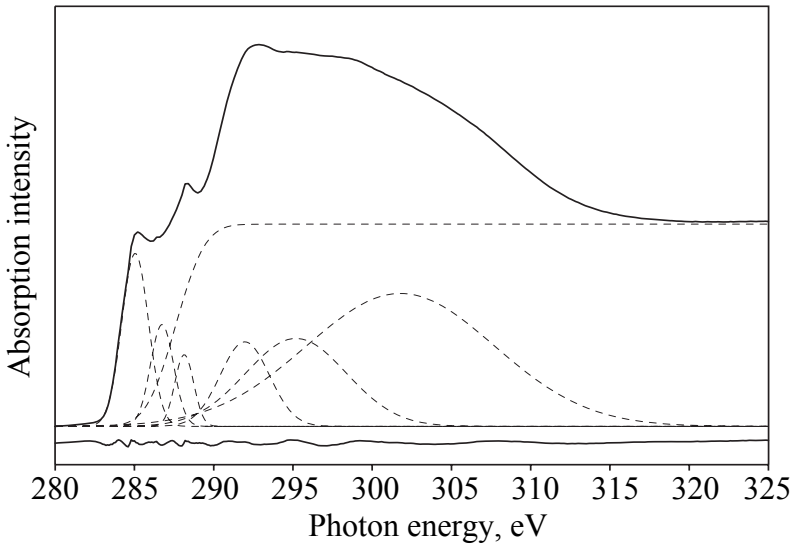

Figure 20 Fitted C1s absorption spectrum of a-CN#1

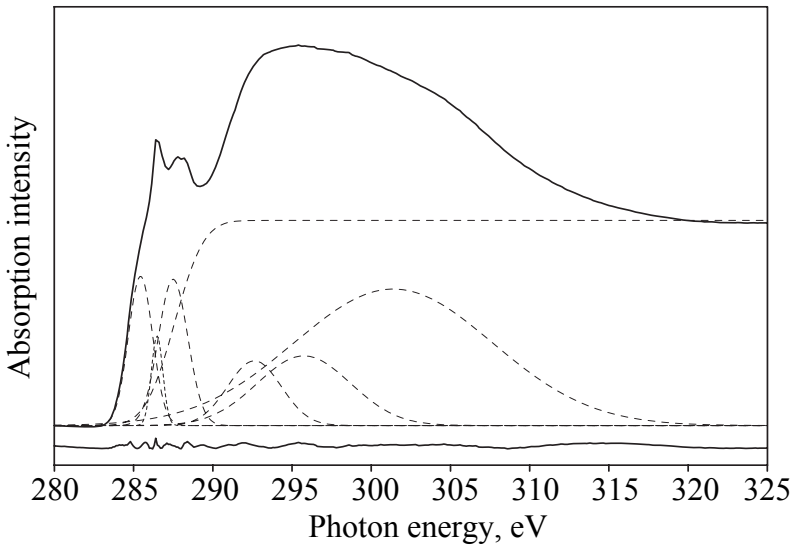

Figure 21 Fitted C1s absorption spectrum of a-CN#2

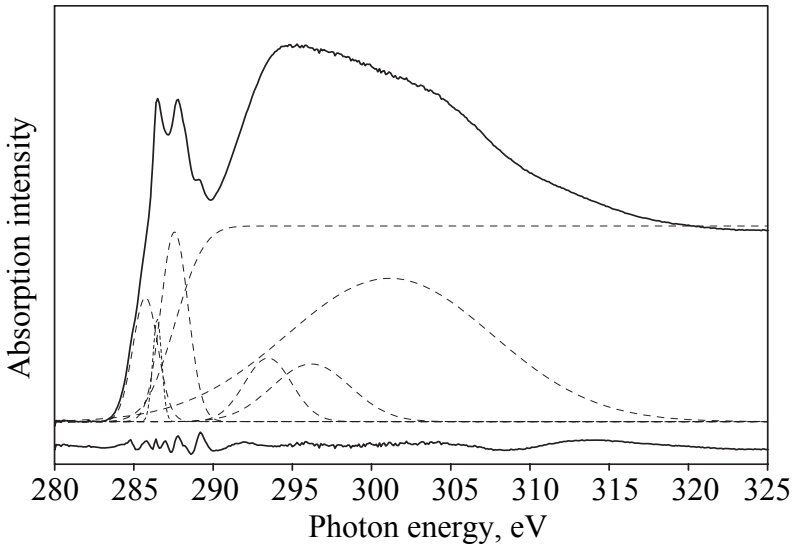

Figure 22 Fitted C1s absorption spectrum of a-CN#3

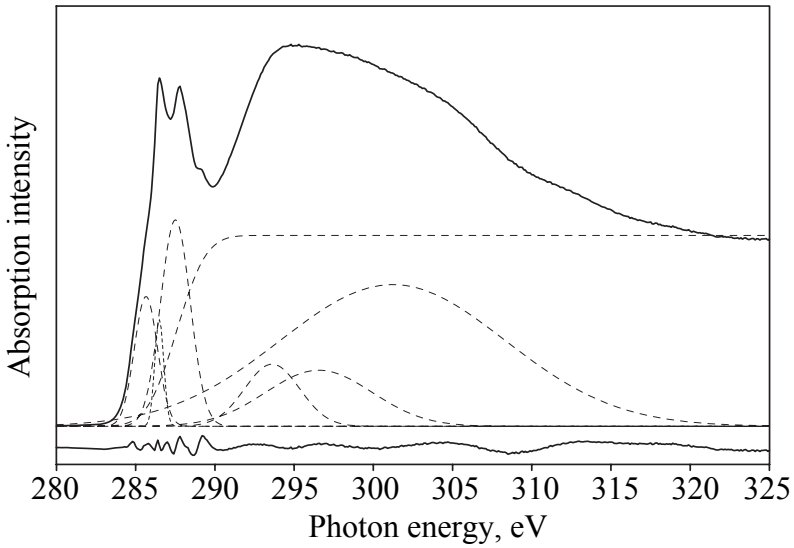

Figure 23 Fitted C1s absorption spectrum of a-CN#4

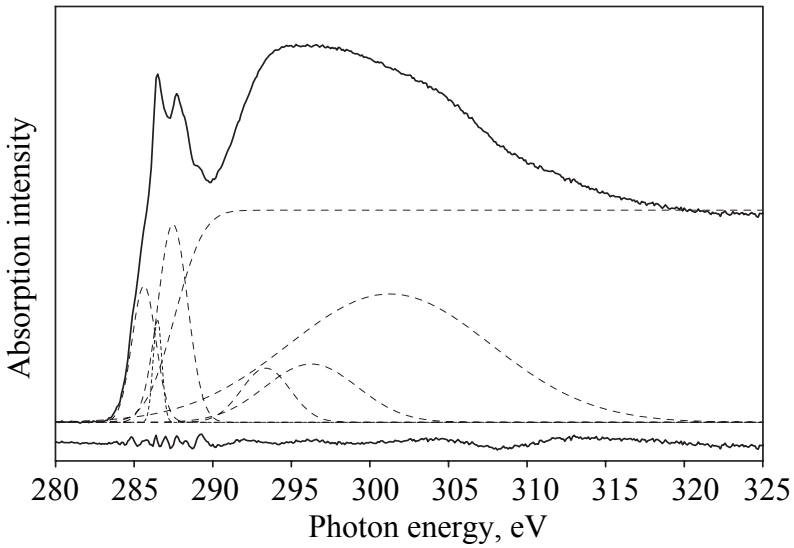

Figure 24 Fitted C1s absorption spectrum of a-CN#5

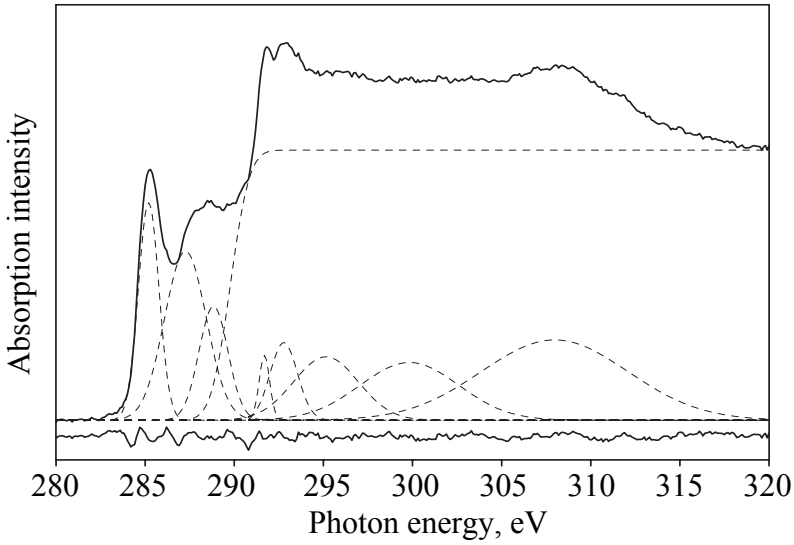

Figure 25 Fitted C1s absorption spectrum of μc-graphite

N1s absorption spectra of a-CN#1 – a-CN#5 were also measured (Figure 26). These spectra did not show significant difference between them which means that hybridization of nitrogen atoms did not change with changing [N]/[C] ratio. Unlike carbon, nitrogen forms a greater variety of bonding configurations and quantitative analysis of the actual hybridization states of nitrogen atoms is left beyond the scope of the current work.

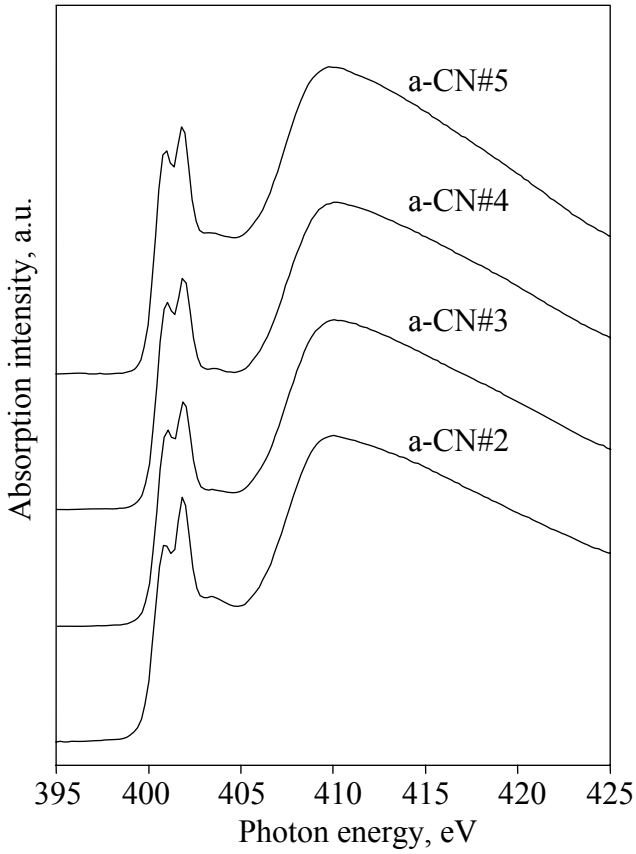

Figure 26 N1s absorption spectra of a-CN films

3.4 Infrared absorption and Raman spectroscopy

3.4.1 Introduction

Infrared absorption and Raman spectroscopy are techniques for studying vibrational modes in condensed matter which helps to identify the types of bonds present in the system. Most of fundamental vibrational modes in condensed matter lie in the energy range that corresponds to middle infrared part of electromagnetic spectrum with wavenumbers from 500 to 4000 cm^{-1}. Corresponding wavelengths are large enough compared to interatomic distances, so dipole approximation can be used. In infrared spectroscopy, vibrations are excited due to absorption of infrared photons by dipoles composed of two adjacent atoms. Not all materials are good IR absorbers, but only those having non-zero local dipole moment which is typical, for example, for systems containing polar bonds of ionic type. Another requirement for vibrational mode to be IR-active is that dipole moment must change as a result of photon absorption and creation of vibrational excitation.

In Raman spectroscopy, different mechanism (Raman effect) is used for excitation of vibrational modes. Raman effect can be interpreted as inelastic scattering of light due to superposition of skeletal vibrations and dipole oscillations induced by electric field of the incident wave. Mathematically, polarizability (α) is a proportionality coefficient between electric field (***E***) and induced dipole moment (***p***),

$$\vec{p} = \alpha \vec{E} \,. \tag{23}$$

In general, polarizability may be affected by skeletal vibrations. So, it may thought of as a function of vibrational coordinate q_i. Near equilibrium point $q_i=0$, polarizability may be approximated by power series,

$$\alpha(q_i) = \alpha(0) + \left(\frac{\partial \alpha}{\partial q_i}\right)_0 q_i + \ldots \tag{24}$$

Assume that vibrations follow harmonic law $q_i=q_o cos(\omega_i t+\delta_i)$ with amplitude q_o, frequency ω_i, and δ_i being the phase determined by initial position of oscillating center. Electric field of the incident wave also oscillate harmonically in time with amplitude E_o and frequency ω, $E=E_o cos(\omega t)$. Substituting this into Equation (23) we obtain the expression for induced dipole moment,

$$p(t) = \left[\alpha(0) + \left(\frac{\partial \alpha}{\partial q_i}\right)_0 q_{io}\cos(\omega_i t + \delta_i)\right] E_o \cos(\omega \cdot t) = \alpha(0) E_o \cos(\omega \cdot t) +$$

$$\frac{1}{2}\left(\frac{\partial \alpha}{\partial q_i}\right)_0 E_o q_{io} \cos[(\omega - \omega_i)t + \delta_i] + \frac{1}{2}\left(\frac{\partial \alpha}{\partial q_i}\right)_0 E_o q_{io} \cos[(\omega + \omega_i)t + \delta_i]. \tag{25}$$

Beside the initial frequency of electromagnetic wave ω, two satellites $(\omega-\omega_i)$ and $(\omega+\omega_i)$ appear in the spectrum. They are referred to as Stocks and anti-Stocks terms respectively. Anti-Stocks scattering is much less intense, because it requires presence of vibrationally excited states while number of those is exponentially small according to Boltzman distribution. It should be mentioned, that inelastic scattering is not coherent because phases of oscillations of different nuclei are not necessarily the same. It can be concluded directly from the Equation (25) that vibrational mode is Raman active if it affects

the local polarizability, or in other words, if $\frac{\partial \alpha}{\partial q_i} \neq 0$. The requirements for obtaining a good response of the system in IR absorption and in Raman spectroscopy are different, which makes the two methods complementary to each other in many cases.

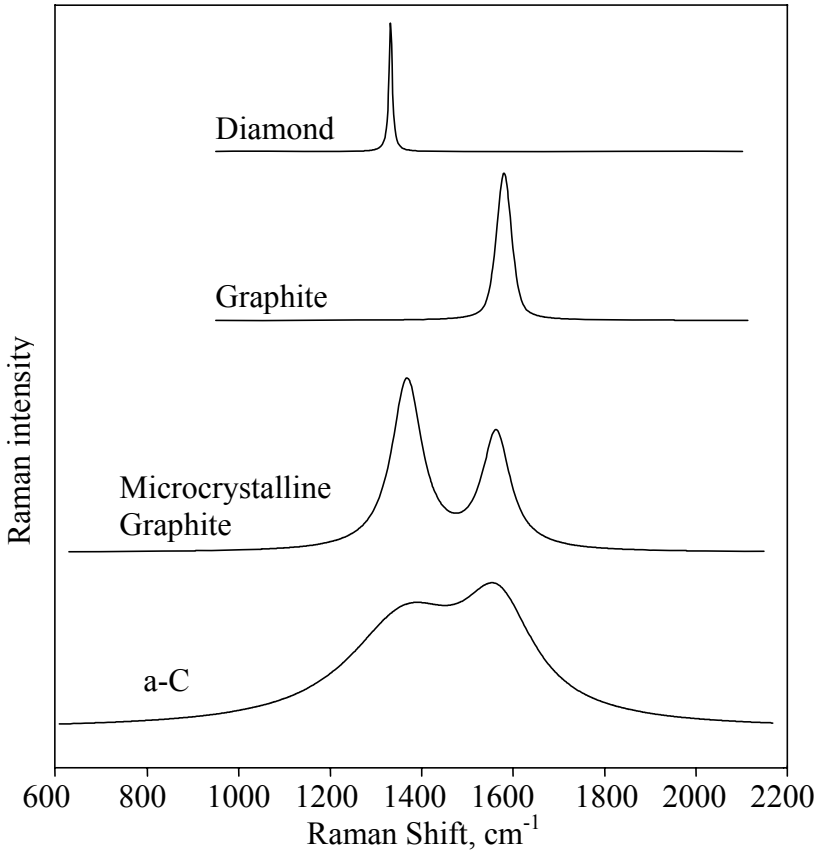

Figure 27 Typical Raman spectra of various carbon materials (Robertson, 2002)

Before going into practical considerations, it is useful to give an idea of how infrared and Raman spectra of various carbon-based systems look in general (Figure 27). Diamond and graphite both have crystalline structure made of covalently bonded carbon atoms, and therefore, as discussed above, do not show significant IR absorption. On the contrary,

Raman spectra of diamond and graphite are very prominent because stretching and contraction of the bond changes the interactions between electrons and nuclei, thereby changing the electronic polarizability. Shorter wavelengths are required to produce the effect, because electron motion has characteristic frequencies corresponding to those of visible or ultraviolet light.

Raman spectroscopy is the most powerful technique for assessing the structural quality of diamond and graphite. Diamond has a single Raman active mode at 1332 cm^{-1} corresponding to the Brillouin zone centre and originating from stretching vibrations of any C-C pair. Graphite mono-crystal has a single Raman active mode, which is zone centre mode at 1580 cm^{-1} labelled "G" for graphite. Disordered graphite has a second mode at around 1350 cm^{-1} labelled "D" for "disorder". It corresponds to breathing vibrations of rings at the graphitic cluster boundary (Figure 24).

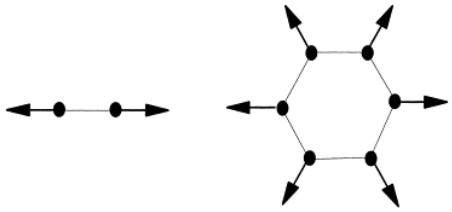

Figure 28 Eigenvectors of the Raman G and D modes in graphite and disordered carbons
(Robertson, 2002)

An unusual and significant fact is that the Raman spectra of most disordered carbons remain dominated by these two G and D modes of graphite, even when the carbons do not have particular graphitic ordering or contain doping elements such as hydrogen and nitrogen.

Raman peaks of diamond and mono-crystal are very sharp. In case of microcrystalline graphite, G and D peaks look broader; and even broader are those of amorphous carbons. It is also should be mentioned, that for amorphous carbons only sp^2 sites are seen in Raman spectrum because their scattering cross-section is 50-230 times larger than that of sp^3 sites (Shroder *et al*., 1990).

3.4.2 Experiment, results, and discussion

Raman spectra were recorded using Renishaw system (model 2000) equipped with 514 nm Ar^+ laser. Shown in Figure 29 are spectra of films with different nitrogen doping level. All spectra were dominated by well known "G" and "D" peaks. Both peaks were quite broad, which is typical for amorphous carbon-based materials. Their relative intensities did not change significantly with increase of doping level, which suggests that carbon substitution by nitrogen did not remarkably change vibrational modes. Additional peak corresponding to carbon-carbon or carbon-nitrogen triple bonds was observed at about 2200 cm^{-1}. This peak was very weak in all spectra, which means that the relative amount of sp^1-bonded carbon was low.

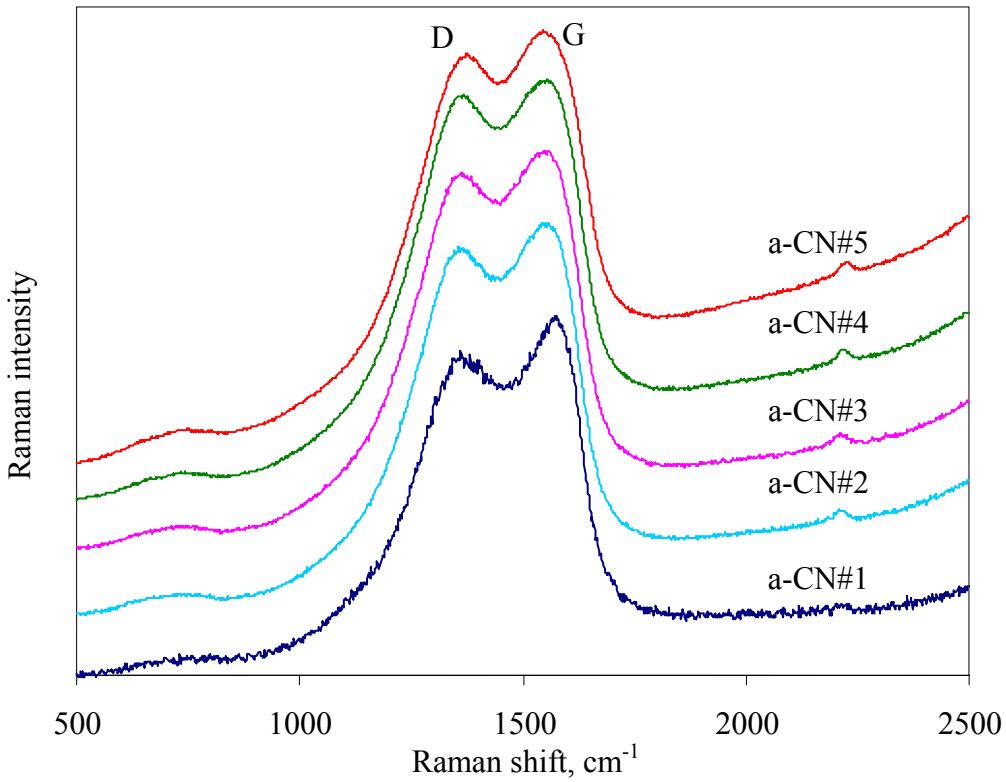

Figure 29 Raman spectra of a-CN films

FTIR spectra were taken in transmission geometry using Si-based samples. The strong infrared absorption of PTFE makes it impossible to take transmission FTIR spectra of films deposited onto PTFE. On the contrary, silicon is transparent enough in infrared region, and silicon background can be easily subtracted from spectra. FTIR spectra of nitrogen-doped carbon films (Figure 30) showed strong activity in the region 1000–1800 cm^{-1}. The IR absorption in this range covers the frequency range of stretching vibration of carbon-carbon and carbon-nitrogen single and double bonds. It was suggested by Kaufman *et al*. (1989) that carbon-carbon bonds become IR-active due to symmetry braking after nitrogen incorporation into graphitic six-fold rings. However, due to absence of reliable information about sub-peak positions and general featurelessness of this broad band, it seems rather not

possible to segregate the contributions of different bond types. Additional bands were observed between 2150 cm^{-1} and 2250 cm^{-1}, which were assigned to the stretching vibration of sp^1 –hybridized nitrile -C≡N and iso-nitrile $–N^{+}≡C^{-}$ groups respectively. Intensity of these band was low, which is consistent with our hypothesis drown from Raman spectra that the relative amount of sp^1-bonded carbon was low.

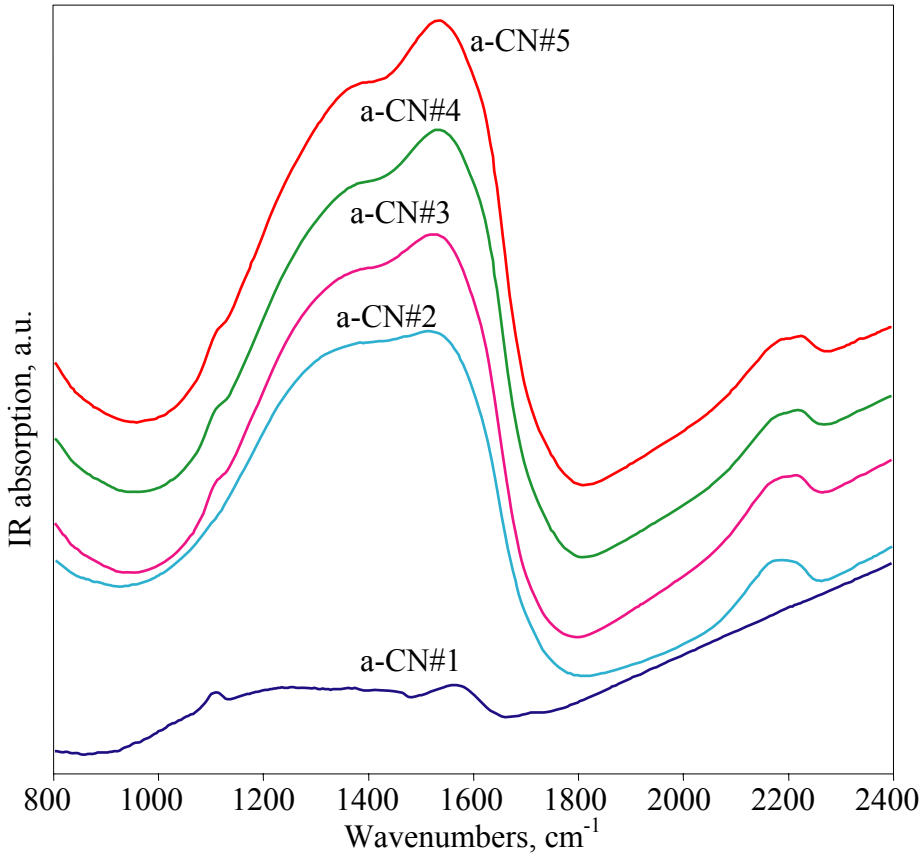

Figure 30 FTIR spectra of a-CN films

3.5 SEM and AFM

3.5.1 Introduction

For high-resolution surface investigations, two commonly used techniques are Atomic Force Microscopy (AFM) and Scanning Electron Microscopy (SEM). The operation of the SEM consists of applying a voltage between a conductive sample and filament, resulting in electron emission from the filament to the sample. This occurs in a vacuum environment ranging from 10^{-4} to 10^{-10} Torr. The electrons are guided to the sample by a series of electromagnetic lenses in the electron column. The electrons interact with the sample within a few nanometers to several microns of the surface, depending on beam parameters and sample type. Electrons are emitted from the sample primarily as either backscattered electrons or secondary electrons. Secondary electrons are the most common signal used for investigations of surface morphology. They are produced as a result of interactions between the beam electrons and weakly bound electrons in the conduction band of the sample. Once these electrons escape from the sample surface, they are detected by scintillator-photomultiplier. The SEM image formed is the result of the intensity of the secondary electron emission from the sample at each (x,y) data point during rastering of the electron beam across the surface.

One of the distinguishing features of the SEM is its larger depth of focus with respect to other types of microscopy. This makes it possible to image very rough surfaces with millimeters of vertical information within a single image. But, at the same time, this makes SEM measurements essentially two-dimensional.

AFM provides three-dimensional surface topography with high resolution on insulators and conductors. It consists of scanning a sharp tip on the end of a flexible cantilever across the sample surface, while maintaining a small, constant interaction force. The tip-sample interaction is monitored by reflecting a laser beam off the back of the cantilever into a split photodiode detector (Figure 31).

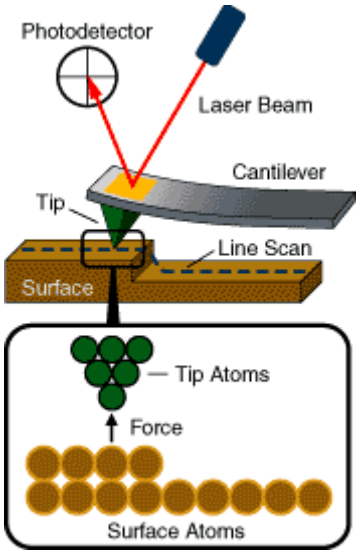

Figure 31 AFM probe setup and operation
(From http://www.molec.com)

The lateral resolution of the image can be as small as the tip radius (typically 2-20 nm, depending on the tip type), and the vertical resolution can be as small as 0.1 nm. The two most commonly used modes of operation are Contact Mode AFM and Tapping Mode AFM. In contact mode, a feedback loop maintains a constant cantilever deflection by vertically moving the scanner to maintain constant photodetector difference signal. The distance the scanner moves vertically at each (x,y) data point is stored by the computer to form the

topographic image of the sample surface. Tapping mode consists of an oscillating cantilever at its resonance frequency and a tip lightly tapping on the surface during the scan. A feedback loop maintains a constant oscillation amplitude by moving the scanner vertically at every (x,y) data point. Recording this movement forms the topographical image. Tapping Mode enables to image soft, fragile, and adhesive surfaces without damaging them, which can be a drawback of contact mode (Russel *et al*., 2001).

3.5.2 Results

AFM pictures of virgin and a-C coated PTFE are shown in Figure 32. Measurements were done using tapping mode AFM in Saskatchewan Structural Science Center (SSSC). Uncoated PTFE surface had a complex fibril-like structure with fiber characteristic size of about 500 nm and surface roughness of about 100 nm. Coating makes it remarkably smoother, which was found out by measuring cross-section.

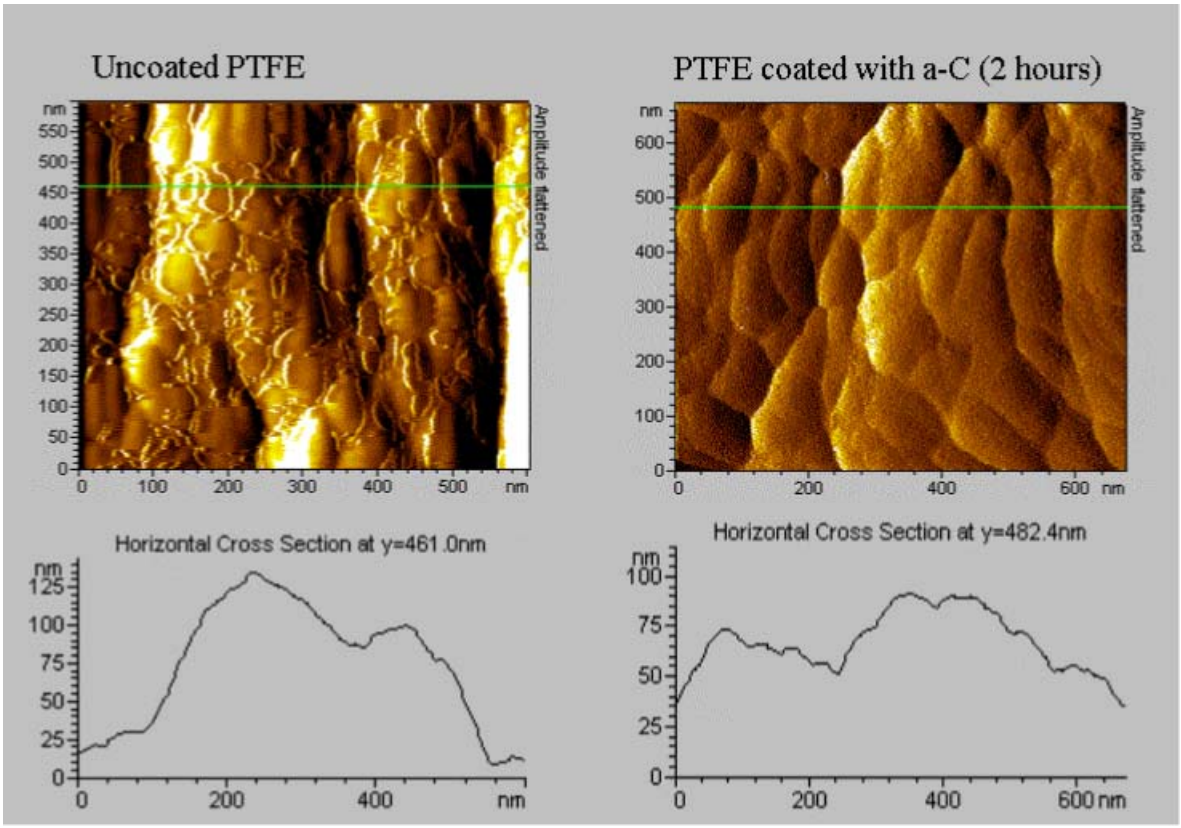

Figure 32 AFM images of virgin and coated PTFE

The ability of AFM as imaging technique to handle irregularities with low aspect ratio makes it possible to measure the thickness of coating on the silicon surface. That was proven in our experiments and used to estimate the changes in deposition rate of a-CN films in various discharge conditions. For the purpose of measuring thickness of coating, the film was removed from a part of silicon wafer using surgical blade. Thus, a measurable step was created. (It should be noted, that hardness of silicon mono-crystal is greater than that of stainless steel which surgical blade is made of. So, silicon surface was not damaged). After that, AFM scanner tip was positioned in the vicinity of the step using micro camera attached to AFM scanner. Figure 33 shows the image of scanned area near the step and the step

measured in cross-section. This method allows estimating the step height with precision not worse than 10%.

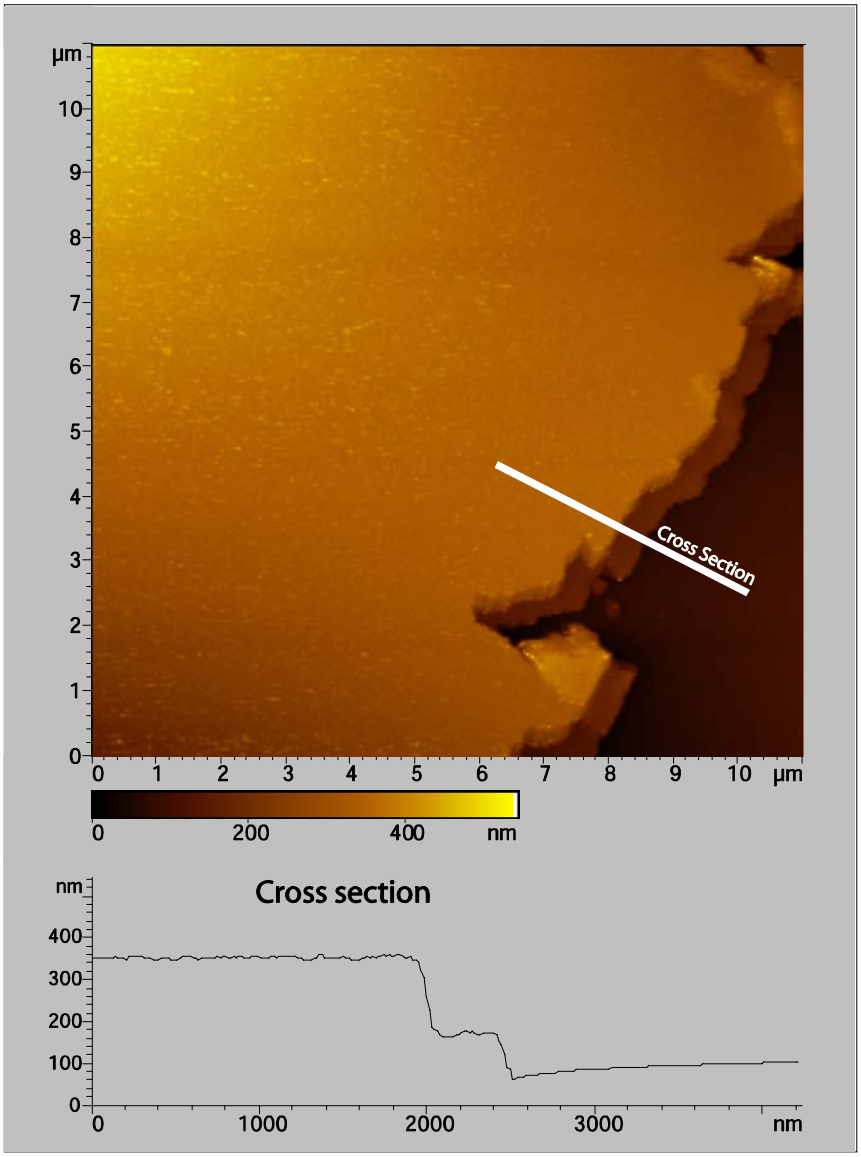

Figure 33 AFM images of measurements CN film thickness on the silicon surface

It was found that film deposition rate increases from about 2 nm/min to about 6 nm/min when nitrogen partial flow rate into discharge tube increases from 0% to 20% (Figure 34). This result may be explained by increase of temperature of heavy species in the plasma with nitrogen addition, since energy transfer from electrons to diatomic species is more efficient due to the presence of vibrational degrees of freedom.

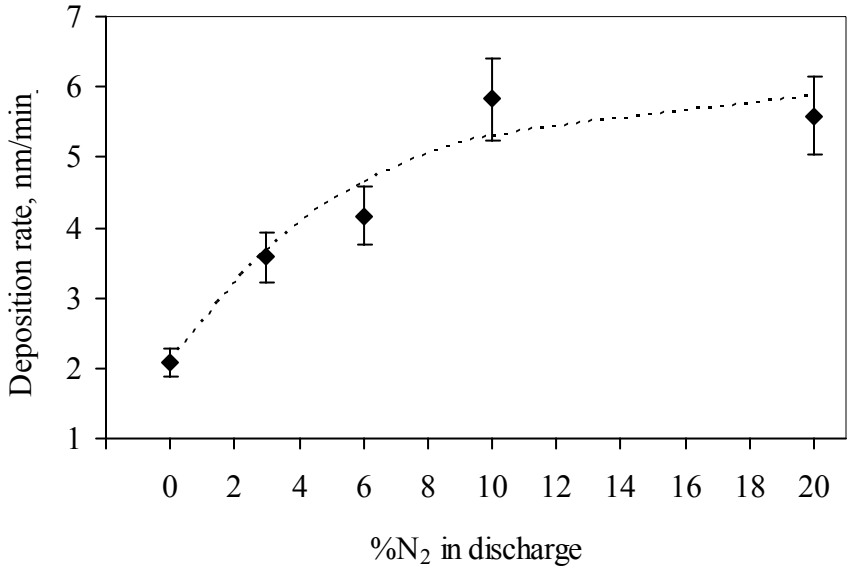

Figure 34 a-CN films growth rates

4. Blood compatibility

4.1 Introduction to blood compatibility and In Vitro testing

Interaction of blood with foreign material can result in two major events from the blood compatibility point of view. The first is blood coagulation (thrombosis); the second is blood tissue damage, i.e. cell death and release of cell contents (hemolysis). One of the most important aspects of blood compatibility is thromboresistance. As mentioned, polymer surfaces enhance blood coagulation and clotting. Mechanism of thrombus formation is complicated and multi-stepped. It includes interaction between blood proteins, cells, and artificial surface (Tirrell et al., 2002). The first step is adsorption of proteins onto surface of vascular graft with formation of layer containing various kinds of proteins. Human blood contains several hundred types of proteins. Their molecular structure and properties can differ significantly. Depending on the properties of material, composition of adsorbed proteins can also be different. The next and most important step involves platelets. Platelets, also known as thrombocytes, along with red blood cells (erythrocytes) and white blood cells (leukocytes) are major blood cells (Figure 35). Platelet adhesion, aggregation and activation with thrombin release and further generation of inter-aggregate fibrin and red cells mesh are sequential steps of thrombus formation. This process is affected by the composition of adsorbed protein layer (Sevastianov, 1991). Some proteins such as fibrinogen, prothrombin, and collagen play a key role in platelet adhesion, activation, and further thrombus formation; others, e.g. serum albumin, can decelerate this process. Therefore, a possible way

to improve hemocompatibility is surface albuminization, i.e. providing such surface properties that stimulate albumin adsorption. Numerous works were done in this area. Relatively high concentration of adsorbed albumin was achieved after exposure of polypropylene to the anhydrous ammonia plasma (Sipehia *et al*., 1986). Strong antithrombotic effect of immobilized heparin due to its binding to antithrombin was demonstrated (Weber *et al*., 2002). These investigations have led to appearance of commercially produced artificial vascular grafts coated with heparin (Begovac *et al*., 2003).

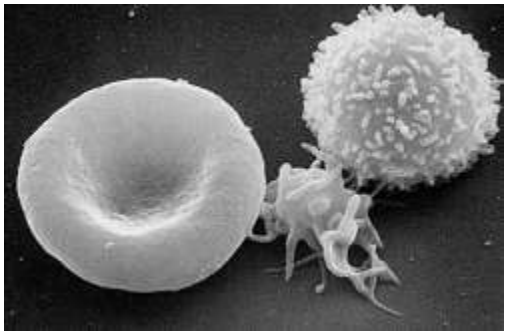

Figure 35 SEM picture of human blood cells
From left to right: erythrocyte, thrombocyte, leukocyte
(Image from http://en.wikipedia.org)

ISO 10993-1, the international standard, provides guidance on the selection of biocompatibility tests for medical devices. It was developed by the International Organization for Standardization (ISO). This standard requires the evaluation of blood compatibility for any medical device that has contact with circulating blood, directly or indirectly. Guidelines for evaluation of blood compatibility are subsequently presented in ISO 10993-4, "Selection of Tests for Interactions with Blood." This standard provides a

structured test-selection system based on the intended use of the device. Although it does not provide detailed test methods or evaluation criteria, it contains useful references.

The evaluation of coated surface usually starts with test for stability of coating following sterilization. Sterilization is a necessary procedure for all implants. A widely used method for sterilization is autoclaving under vapor pressure at 120°C. It is required that sterilization does not damage, remove or modify the coating. The thrombotic potential of surface is usually evaluated by measuring the clot development time in a static situation and comparing to the time for clot development to the same point of maturity for blood drawn simultaneously and exposed to the reference surface (Black, 1999). The reference material is usually silicone-coated soft glass. Although it is not a satisfactory material for implant use due to its poor mechanical properties, this material is perhaps the best inexpensive test material with enviable biological performance and reproducible response. A canine donor is usually used although some investigators have used human donors. Hemolysis can be determined simultaneously in such a static test by centrifugation of the clotted blood followed by optical spectrophotometric determination of the hemoglobin content of the supernatant serum. Also, it is useful to compare the results obtained with a test material and a reference material using blood drawn at one time.

As the absorption and adhesion of coagulation proteins and platelets can greatly affect the thrombogenicity of artificial surfaces, blood compatibility assessment includes analysis of proteins and platelets adhered after contact with blood. Radiolabelling can be used to quantify the total amount of protein of a certain type or platelets on the surface (Cui *et al*.,

2000). Scanning electron microscopy can provide information not only about total amount but also about degree of aggregation and activation of platelets, which is very important.

Thrombus formation is a complicated process in which the precipitation of proteins (fibrinogen, albumin, etc.) and cellular elements (red cells, white cells, and platelets) from the blood onto artificial surfaces occurs in the presence of flow. Correlation between physico-chemical surface properties and blood compatibility is not well understood. Fluorocarbon polymers are strongly hydrophobic, so there can be a net attraction and a strong driving force between the biomaterial surface and hydrophobic domains of proteins. Thus, it is preferable to reduce hydrophobicity. Surface morphology is also important, because for minimizing cell adhesion on blood-contacting biomaterial surface, roughness must be less than cellular dimensions. Besides indirect assessment, in vitro and in vivo tests are required to confirm blood compatibility in a particular case (Black, 1999).

4.2 Review of blood compatibility studies on carbon-based coatings

A number of recent publications address the blood compatibility issues of C and CN coatings. Adsorption of albumin and fibrinogen on DLC and CN-coated PMMA was studied using radioactively tagged proteins (Cui *et al*., 2000). It was shown that DLC coatings exhibit a higher albumin and fibrinogen adsorption compared with CN coating and PMMA control samples. The albumin/fibrinogen ratio was 1.008 for DLC, 0.49 for CN, and 0.39 for PMMA. This result indicates that DLC's blood compatibility is the best among three different surfaces, and CN coating exhibit a slightly better blood compatibility than PMMA. Total number of platelets adhering to the DLC-coated PMMA in that work was three times less than that of control sample. Although results above strongly suggest improved blood compatibility of DLC in vitro, further studies on the effects of N atoms content in coatings on blood compatibility are required.

In other work (Chen *et al*., 2002) effects of sp^3 content in hydrogenated DLC film fabricated using plasma immersion ion implantation and its biocompatibility were studied. It was found that blood compatibility becomes worse at larger sp^3/sp^2 ratio. But this may not be true for hydrogen-free DLC. This question remains to be a subject of future investigation.

Rodil *et al.* (2003) studied the biocompatibility of a-C, a-CN, and a-C:H coatings deposited on stainless steel samples using magnetron sputtering. Biocompatibility tests involved fibroblasts and osteoblasts attachment and proliferation using spectrophotometric techniques for different periods of time. They also studied the influence of surface morphology on cells attachment capability. It was found, that osteoblast cells adhere better to rough surfaces with

irregular morphologies. On the contrary, fibroblasts prefer smooth surfaces rather than roughened ones. The longer-term results (cells proliferation) suggested a better performance of the a-C films compared to a-CN.

Blood clotting behavior and platelets adherence rates on a-CN coated surface were compared to those on 316L stainless steel and NiTi alloy (these materials are often used to fabricate these blood-contacting devices) by Zheng *et al.* (2005). For a-CN with N/C ratio equal to 0.31 the rate of platelet adhesion was found to be the lowest among all a-CN coated surfaces and 1.5 - 2 times lower than that on 316L and NiTi surfaces. Blood clotting rate on a-CN was also less then that on compared surfaces.

Nitrogen and hydrogen are not the only elements that are used for the doping of carbon coatings. In the work of Kwok *et al.* (2005) phosphorus was successively used for that purpose. Coatings were made using PIII-D and platelet adhesion was studied in comparison to low-temperature isotropic pyrolytic carbon (LTIC) and undoped DLC. Total number of adhered platelets on a-CP was found to be 1.5-2 times less then that on LTPC and DLC. However, the activation of platelets expressed different behavior. Best results were obtained for DLC, while LTPC and a-CP did not show remarkable difference between them.

4.3 Results of biocompatibility tests

4.3.1 Platelet adsorption and activation

Blood was obtained from healthy donors taken no medication for at least 10 days prior to the donation and collected in tube containing 3.8% trisodium citrate as anticoagulant. 45ml of blood were centrifuged in one 50 ml tube for 15 min at 890 rpm (200 g) at room temperature. Platelet rich plasma (PRP) was obtained (upper solution). A suspension of $3 \cdot 10^8$ platelets/ml was labeled with 300 μCi of Cr^{51} at room temperature for 30 minutes. Then the suspension was rinsed twice with buffer solution (phosphate buffered saline, PBS) to remove the unbounded Cr^{51}. 50 μl of the labeled suspension were incubated with the coated surfaces for 2 hours at 37°C. The samples were then rinsed twice with PBS and the number of adherent platelets was measured using a gamma scintillation counter.

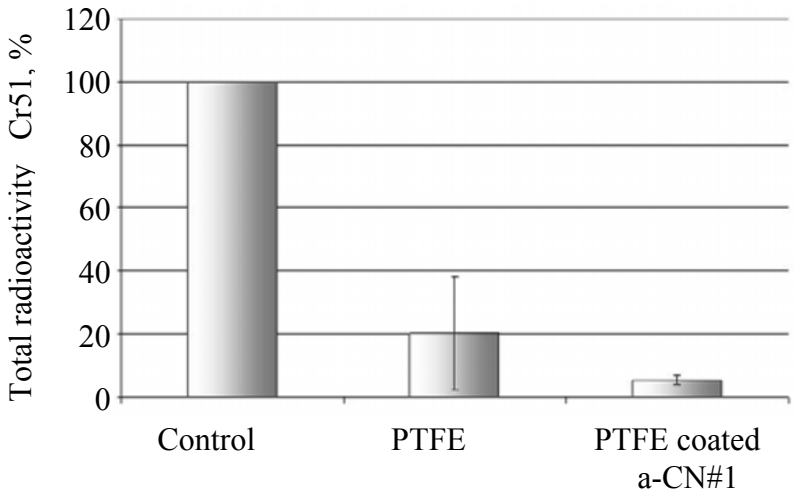

Figure 36 Results of radio-labeled platelet adsorption

Results of adsorbed platelet counting on a-CN#1 are shown in Figure 36. From this figure one can conclude that the number of platelets adsorbed on the coated surface is less than that on the bare PTFE. However, statistical analysis showed no significant difference between them.

Platelet activation was studied using SEM. Platelet rich plasma obtained by centrifugation of peripheral human blood was used in those experiments. 50 μl of PRP were placed on the coated and virgin PTFE surface for 2 hours at 37°C. SEM pictures showing the results of platelets activation are presented in Figure 37. From those pictures, we can see that the total number of platelets adhered was not much different for virgin and coated surface. But, platelets on the coated surface were much less aggregated and less activated.

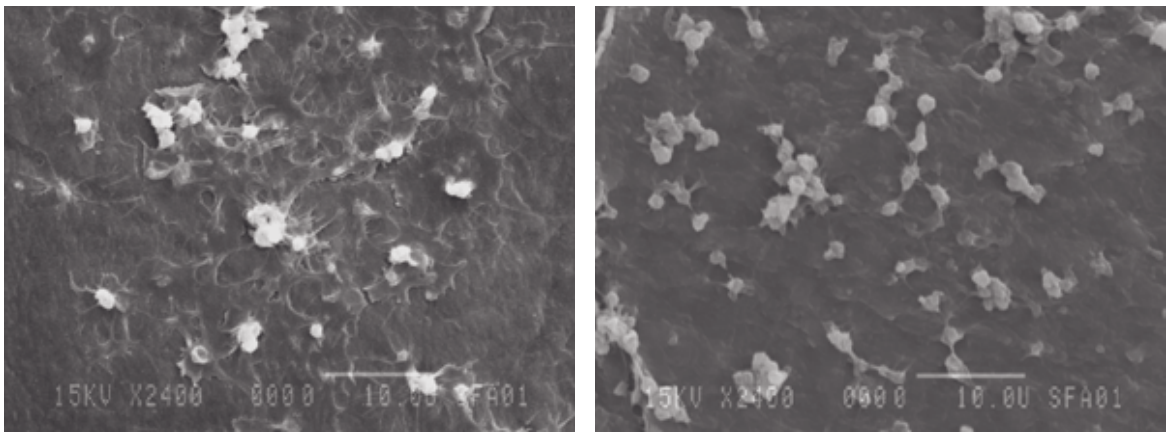

Figure 37 SEM pictures of platelets on virgin and a-CN#1 coated PTFE surface.

(Uncoated PTFE is on the left, coated PTFE is on the right).

Quantitative analysis of platelet aggregation and activation was also performed. Degree of platelet aggregation and activation was estimated from their morphology. Adhesion process

is believed to run in four stages: platelet attachment to the surface, activation, pseudopodia development, spreading, and aggregate formation. According to this, four morphological classes are usually used to classify platelets:

I. Single non-activated cells.

II. Slightly activated cells with pseudopodia.

III. Spread (fully spread platelets).

IV. Aggregated (aggregates of two or more platelets).

Usual approach for quantitative investigation of platelet adhesion consists of calculation of relative index of platelet adhesion (RIPA) for different morphological classes of adhered platelets. Shown in Figure 38 are RIPA values for a-CN#1 – a-CN#5 coatings and for untreated PTFE.

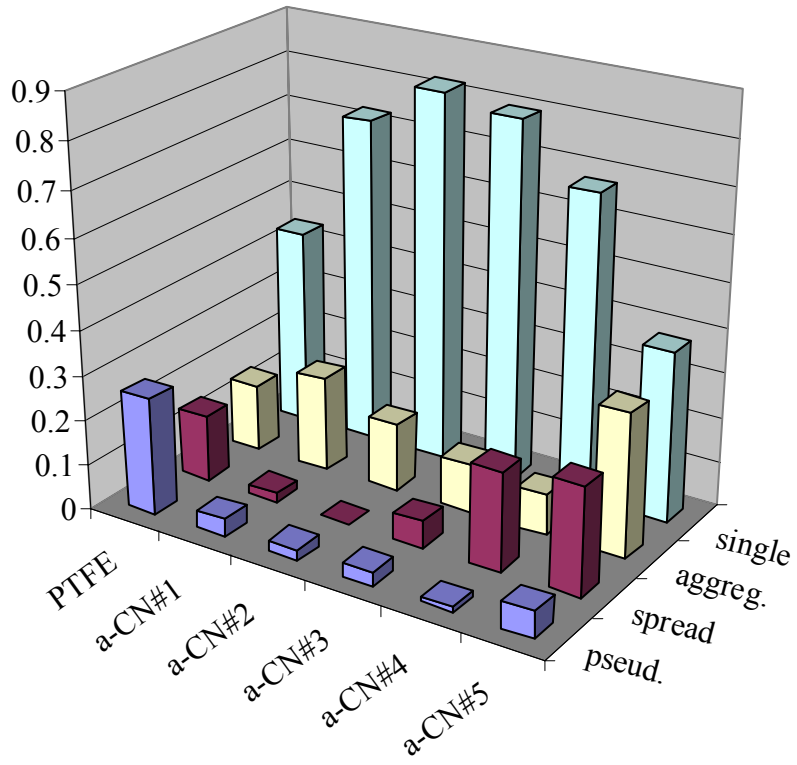

Figure 38 Relative indexes of platelet adhesion

It may be concluded from Figure 38 that the best result (lowest degree of platelet activation) was achieved for a-CN#2 which corresponds to the partial N_2 flow into the discharge tube equal to 3%. Excessive nitrogen enhances platelet activation and reduces blood compatibility. Thus, sample a-CN#5 showed almost the same platelet activation as uncoated PTFE.

4.3.2 Endothelial and smooth muscle cells adherence

Cytotoxicity, another extremely important parameter, was studied also. Cells attachment to artificial surface is a good indicator of low cytotoxicity. Fibroblasts and endothelial cells were chosen for this type of tests, as they are the main cells of the blood vessel wall tissue. Endothelial cells were obtained from umbilical human vein, and fibroblasts were obtained commercially. Cells were exposed to the surface for 48 hours at 37°C, and after that specimens were investigated with SEM. No cells attachment was observed on virgin PTFE surface. On the contrary, coated surfaces showed good cell attachment with formation of focal contacts and good spreading. Results are shown in Figure 39.

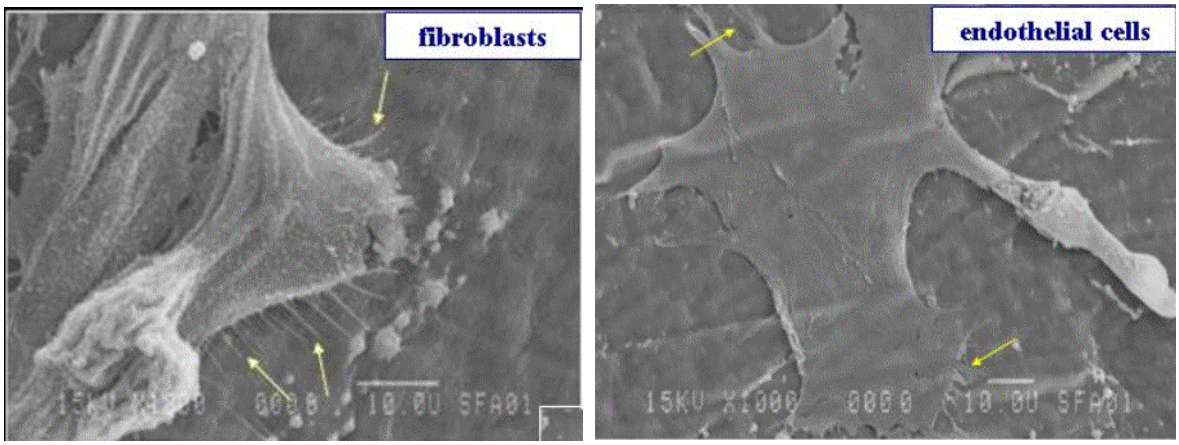

Figure 39 SEM pictures of fibroblasts and endothelial cells on a-CN#1 coated PTFE

4.3.3 Neutrophils adsorption

Neutrophils are characteristic of the inflammatory response of an individual to a foreign material and this can be considered to be dependent on how close the material mimics the natural (extracellular) environment of the cell. In order to explore neutrophils adsorption, blood was obtained using the same procedure as described in Section 3.1 of this Chapter. The upper suspension was used to obtain platelets rich plasma, as previously described. The bottom leukocyte rich suspension was used to extract neutrophils using the Ficoll-Paque technique. A suspension of $3 \cdot 10^8$ neutrophils was labeled with 300 μCi of In^{111} for 30 minutes at room temperature. Then the suspension was rinsed twice with PBS to remove the unbounded In^{111}. 100 μl of the labeled suspension were incubated with coated surfaces for 2 hours at 37°C. The samples were then rinsed twice with PBS and the number of absorbed neutrophils was measured using a gamma scintillation counter.

Results shown in Figure 40 do not demonstrate remarkable increase in neutrophils adsorption to coated surface. Thus, there is no evidence that coating is expected to reduce the inflammation that may occur as a part of organism response to a foreign body.

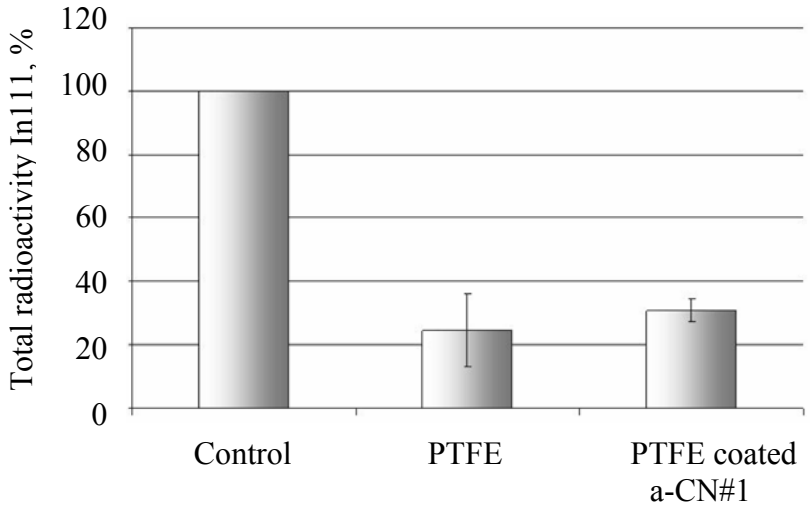

Figure 40 Neutrophils adsorption

4.3.4 Whole blood contact

Adhesion of blood cells as well as the formation of fibrin on the sample surface was investigated by SEM. Immediately after collection blood was incubated on the surfaces for 30 minutes at 37°C. Then, the samples were washed twice with PBS to remove the non-adherent cells from the surface and SEM analysis was applied. SEM pictures are shown in Figure 41. Coated surface (Figure 41 A and B) showed a little amount of fibrin and virtually no red cells attachment. But uncoated surface (Figure 41 C and D) had a large number of red cells entrapped in the fibrin net. Correlating these data with the time required for fibrin formation, we can suppose that, even if the time is not significantly different, fibrin do not

strongly attach on treated PTFE. Thus, from this point of view, the surface after the coating is less thrombogenic than the uncoated PTFE.

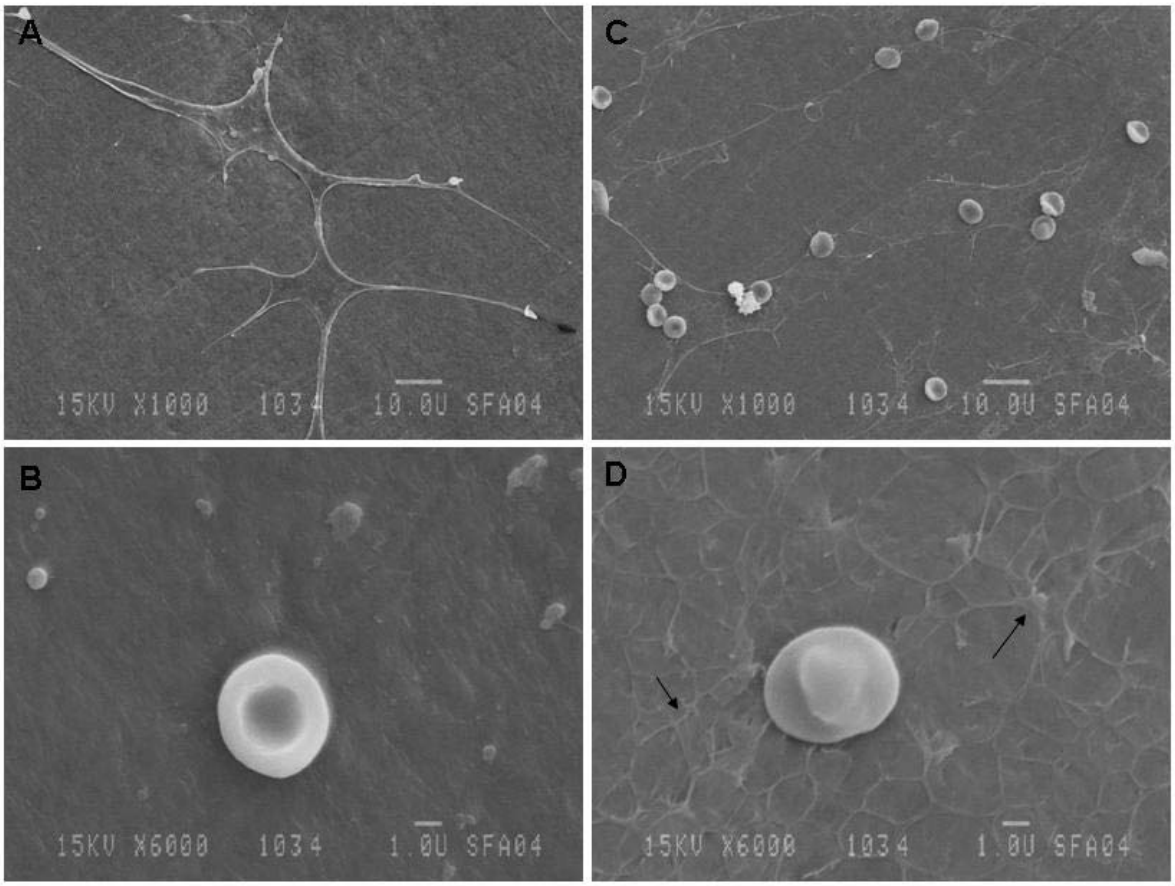

Figure 41 SEM analysis after whole blood contact with a-CN coated PTFE (A, magnification 1000x), (B, magnification 6000x) and virgin

(C, magnification 1000x), (D, magnification 6000x).

Arrows indicate the fibrin net on the material surface

5. Summary

Amorphous nitrogenated carbon coatings with varying nitrogen content were successfully produced using hot filament DC plasma sputtering of graphite in the mixture of N_2 and Ar gases. Doping level was varied by controlling N_2 partial gas flow rate into the reactor. Five sample standards with deposition time equal to 2 hours and different N_2 partial flow rate were chosen for further experiments (Table 5). Deposition on PTFE and Si wafers was performed simultaneously to enrich the possibilities for further analisys. Thickness of a-CN films on Si wafers was measured with AFM tip going across the step created on surface by scratching the film with stainless steel blade and deposition rates were calculated. Surface atomic composition was studied by XPS. Surface mass densities were estimated from analysis of plasmon peaks measured by EELS. Percentage of sp^2-bonded carbon was estimated from XAS. It was shown by Raman and FTIR spectroscopic measurements that the amount of sp^1-bonded carbon in deposited coatings is negligible. Most important results are summarized in Table 5.

Biocompatibility was assessed by a number of tests including the interaction with whole blood and various cells such as platelets, endothelial cells, neutrophils, fibroblasts. Platelet adsorption did not show statistically significant decrease in total number of platelet adsorbed on the coated surface compared to that adsorbed on bare PTFE. However, platelets on coated surface were much less aggregated and activated. Quantitatively, activation of

platelets was studied in terms of relative index of platelet activation. The best RIPA were obtained for the sample a-CN#2.

Table 5. Summary of physico-chemical properties of a-CN coatings

Sample identification	$\%N_2$ in discharge	Thickness, nm	Deposi-tion rate, nm/min	Surface atomic % [N]	Surface atomic % [O]	Surface mass density	$\%sp^2$ bonded carbon
a-CN#1	0%	252	2.1	7.9%	14.8%	2.43	67%
a-CN#2	3%	420	3.5	23.9%	12.3%	2.52	72%
a-CN#3	6%	480	4.0	28.9%	12.7%	2.65	76%
a-CN#4	10%	696	5.8	29.6%	12.6%	2.70	81%
a-CN#5	20%	624	5.2	30.7%	10.2%	2.70	80%

From qualitative SEM studies it was found that coated surface stimulates endothelial cells and fibroblasts attachment and proliferation. At the same time, cells attachment to uncoated PTFE is negligible. Inflammatory response of PTFE is not likely much reduced by coating as followed from experiments with neutrophils adsorption. But in spite of that, overall results of blood test were encouraging. Experiments with whole blood showed a good antithrombogenic potential of amorphous CN coatings. Conclusion was made, that this type of coatings seems generally able to improve the biological performance of PTFE if the amount of nitrogen dopant is properly adjusted.

List of references

Aisenberg, S., Chabot, R., Ion-beam deposition of thin films of diamond-like carbon. *Journal of Applied Physics*, 1971. 42(7): p. 2953-2958.

Begovac, P.C., Thomson, R. C., Fisher, J. L., Hughson, A., Gallhagen, A., Improvements in GORE-TEX® Vascular Graft Performance by Carmeda® BioActive Surface Heparin Immobilization. *European Journal of Vascular and Endovascular Surgery*, 2003. 25: p. 432-437.

Bhushan, B., Chemical, mechanical and tribological characterization of ultra-thin and hard amorphous carbon coatings as thin as 3.5 nm: recent developments. *Diamond and Related Materials*, 1999. 8: p. 1985-2015.

Black, J., Biological performance of materials: fundamentals of biocompatibility. 1999, New York: Marcel Dekker.

Bruhwiler, P.A., Karis, O., Martensson, N. Charge-transfer dynamics studied using resonant core spectroscopies. *Reviews of Modern Physics*, 2002. 74: p.703-740.

Bubert, H. and Jenett, H. (Editors). Surface and thin film analysis: Principles, instrumentation, and applications. 2002, Wiley-VCH Verlag GmbH.

Chen, J.Y., L.P. Wang, K.Y. Fu, N. Huang, Y. Leng, Y.X. Leng, P. Yang, J. Wang, G.J. Wan, H. Sun, X.B. Tian, P.K. Chu, Blood compatibility and sp^3/sp^2 contents of diamond-like carbon (DLC) synthesized by plasma immersion ion implantation-deposition. *Surface & Coatings Technology*, 2002. 156: p. 289-294.

Conrads, H., Schmidt, M. Plasma generation and plasma sources. *Plasma Sources Science and Technology*, 2000. 9: p. 441-454.

Cui, F.Z., Li, D.J., A review of investigations on biocompatibility of diamond-like carbon and carbon nitride films. *Surface & Coatings Technology*, 2000. 131: p. 481-487.

Diaz, J., Anders, S., Zhou, X., Moler, E., Kellar, S., Hussain, Z., Analysis of the π^* and σ^* bands of the x-ray absorption spectrum of amorphous carbon. *Physical Review B*, 2001. 64: p.125204.

Hamilton, T. Determining the sp2/sp3 bonding concentrations of carbon films. M.Sc. Thesis, University of Saskatchewan, June 2005.

Hamilton, T., Foursa, M., Hirose, A., Moewes, A. X-ray absorption of nitrogen-doped amorphous carbon films for determining sp^2/sp^3 bonding concentrations, *Radiation Physics and Chemistry*, 2006. 75 (11): p. 1613.

Henke, B.L., Gullikson, E.M., and Davis, J.C. X-Ray Interactions: Photoabsorption, Scattering, Transmission, and Reflection at E = 50–30,000 eV, Z = 1–92. *Atomic Data and Nuclear Data Tables* **54,** 181 (1993)

Hofsass, H., Binder, H., Klumpp, T., Recknagel, E., Hydrogen-free amorphous carbon films: correlation between growth conditions and properties. *Diamond and Related Materials*, 1994. 3(1-2): p. 137-142.

Kaufman, J., Metin, S., Saperstein, D., Symmetry breaking in nitrogen-doped amorphous carbon: Infrared observation of the Raman-active G and D bands. *Physical Review B*, 1989. 39(18): p. 13053-13060.

Krause, M.O. Atomic radiative and radiationless yields for K and L Shells. *Journal of Physical and Chemical Reference Data*, 1979. 8: p. 307.

Kwok, S.C.H., Wang, J., and Chu, P.K. Surface energy, wettability, and blood compatibility phosphorus doped diamond-like carbon films. *Diamond and Related Materials*, 2005. 14(1): p. 78-85.

Lieberman, M.A., Liehtenberg, A.J., Principles of plasma discharges and materials processing. 1994, New York: John Willey & Sons.

Ponomarev, A., Vasilets,V., Kinetics and mechanisms of chemical interaction of low-temperature plasma with polymers, in *Encyclopedia of low-temperature plasma* (in russian), V. Fortov (Editor). 2000, Nauka: Moscow. p. 374-382.

Powell, C.J., Jablonski, A., Tilinin, I.S., Tanuma, S., and Penn D.R. Surface sensitivity of Auger-electron spectroscopy and X-ray photoelectron spectroscopy. *Journal of Electron Spectroscopy and Related Phenomena*, 1999. 98-99: p.1-15.

Prieto, P., Quiros, C., Elizalde, E., and Sanz, J.M. Quantitative REELS of amorphous carbon and carbon nitride films. *Surface and Interface Analysis*, 2004. 36: p. 820–823.

Robertson, J., Diamond-like amorphous carbon. *Materials Science and Engineering R*, 2002. 37: p. 129-281.

Rodil, S.E, Olivares, R., Arzate, H., and Muhl, S. Properties of carbon films and their biocompatibility using in-vitro tests. *Diamond and Related Materials*, 2003. 12(3-7): p. 931-937.

Russel, P., Batchelor, D., Thornton, J., SEM and AFM: Complementary techniques for high resolution surface investigations. *Microscopy and Analysis*, 2001(July): p. 9-12.

Schwan, J., Ulrich, S., Roth, H., Ehrhardt, H., Silva, S.R.P., Robertson, J., Samlenski, R., Brenn, R., Tetrahedral amorphous carbon films prepared by magnetron sputtering and DC ion plating. *Journal of Applied Physics*, 1996. 79(3): p. 1416-1422.

Seah, M., Dench, W. Quantitative electron spectroscopy of surfaces: a standard data base for electron inelastic mean free paths in solids. *Surface and Interface Analysis*, 1979. 1(1): p. 2-11.

Sevastianov, V.I., Interrelation of protein adsorption and blood compatibility of biomaterials, in *High performance biomaterials: A comprehensive guide to medical and pharmaceutical applications*, M. Szycher (ed.) 1991, Lancaster: Technomic. p. 313-341.

Sherwood, P.M.A., in: Briggs, D., Seah, M.P. (Eds.), Practical Surface Analysis by Auger and X-ray Photoelectron Spectroscopy, Wiley, Chichester, 1983, Appendix 3.

Shirley, D.A., High-resolution x-ray photoemission spectrum of the valence bands of gold. *Physical Review B*, 1972. 5(12): 4709.

Shroder, R., Nemanich, R., Glass, J., Analysis of the composite structures in diamond thin films by Raman spectroscopy. *Physical Review B*, 1990. 41(6): p. 3738-3745.

Sipehia, R., Chawla, A. S., Chang, T. M. S., Enhanced albumin binding to polypropylene beads via anhydrous ammonia gaseous plasma. *Biomaterials*, 1986. 7(6): p. 471-473.

Skytt, P., Glans, P., Mancini, D.C., Guo, J.-H., Wassdahl, N., Nordgren, J., Ma, Y. Angle-resolved soft x-ray fluorescence and absorption study of graphite. *Physical Review B*, 1994. 50(15): p. 10457-10461.

Tanuma, S., Powell, C.J., and Penn, D.R. Calculations of electron inelastic mean free paths for 27 elements over the 50-2000 eV energy range. *Surface and Interface Analysis*, 1991. 17: p.911-926.

Tirrell, M., Kokkoli, E., Biesalski, M., The role of surface science in bioengineered materials. *Surface Science*, 2002. 500: p. 61-83.

Tougaard, S. and Sigmund, P. Influence of elastic and inelastic scattering on energy spectra of electrons emitted from solids. *Physical Review B*, 1982. 25: p.4452.

Tougaard, S. Quantitative analysis of surface electron spectra: Importance of electron transport. *Surface and Interface Analysis*, 1988. 11 (9): 453-472.

Tougaard, S. Algorithm for analysis of low-energy-resolution REELS; determination of inelastic electron scattering cross-sections and applications in quantitative XPS. *Surface Science*, 2000. 464: p.233-239.

Vegh, J. The Shirley-equivalent electron inelastic scattering cross-section function. *Surface Science*, 2004. 563: p. 183–190.

Voevodin, A., Donley, M., Preparation of amorphous diamond-like carbon by pulsed laser deposition: A critical review. *Surface and Coatings Technology*, 1996. 82(3): p. 199-213.

Waidmann, S., Knupfer, M., Fink, J., Kleinsorge, B., and Robertson, J., Electronic structure studies of undoped and nitrogen-doped tetrahedral amorphous carbon using high-resolution electron energy-loss spectroscopy. *Journal of Applied Physics*, 89 (2001), p. 3783.

Weber, N., Wendel, H.P., Ziemer, G., Hemocompatibility of heparin-coated surfaces and the role of selective plasma protein adsorption. *Biomaterials*, 2002. 23: p. 429-439.

Yeh, J.-J., Lindau, I., Atomic subshell photoionization cross sections and asymmetry parameters: $1 < Z < 103$, *At. Data Nucl. Data Tables*, 1985. 32: p.1.

Yubero, F., Tougaard, S. Model for quantitative analysis of reflection-energy-loss spectra. *Physical Review B*, 1992. 46: p.2486.

Yubero, F., Sanz, J.M., Ramskov, B., Tougaard, S. Model for quantitative analysis of reflection-energy-loss spectra: Angular dependence. *Physical Review B*, 1996. 53: p. 9719.

Zheng, C.L, Cui, F.Z., Meng, B., Ge, J., Liu, D.P., and Lee, I.-S. Hemocompatibility of C-N films fabricated by ion beam assisted deposition. *Surface and Coatings Technology*, 2005. 193(1-3): p. 361-365.